

# Dwarf Galaxy Discoveries from the KMTNet Supernova Program III. the Milky-Way Analog NGC 2997 Group

Tony Junjing Fan,<sup>1</sup> Dae-Sik Moon,<sup>1</sup> Hong Soo Park,<sup>2,3,4</sup> Dennis Zaritsky,<sup>4</sup> Sang Chul Kim,<sup>2,3</sup> Youngdae Lee,<sup>5</sup> Ting S. Li,<sup>1</sup> Yuan Qi Ni,<sup>1</sup> Jeehye Shin,<sup>2,3</sup> Sang-Mok Cha,<sup>2,6</sup> Yongseok Lee,<sup>2,6</sup>

<sup>1</sup>David A. Dunlap Department of Astronomy and Astrophysics, University of Toronto, 50 St. George Street, Toronto, ON M5S 3H4, Canada

<sup>2</sup>Korea Astronomy and Space Science Institute, 776, Daedeokdae-ro, Yuseong-gu, Daejeon 34055, Republic of Korea

<sup>3</sup>Korea University of Science and Technology (UST), Daejeon 34113, Republic of Korea

<sup>4</sup>Steward Observatory, University of Arizona, 933 North Cherry Avenue, Tucson, AZ 85719, USA

<sup>5</sup>Department of Astronomy and Space Science, Chungnam National University, Daejeon 34134, Republic of Korea

<sup>6</sup>School of Space Research, Kyung Hee University, Yongin 17104, Republic of Korea

Accepted XXX. Received YYY; in original form ZZZ

## ABSTRACT

We present the discovery of 48 new and the analysis of 55, including 7 previously discovered, dwarf galaxy candidates around the giant spiral galaxy NGC 2997 using deep *BVI* images from the KMTNet Supernova Program. Their *V*-band central surface brightness and total absolute magnitudes are in the range of 20.3–26.7 mag arcsec<sup>-2</sup> and  $-(8.02-17.69)$  mag, respectively, while the *I*-band effective radii are 0.14–2.97 kpc. We obtain  $\alpha \approx -1.43 \pm 0.02$  for the faint-end slope of their luminosity function, comparable to previously measured values but shallower than theoretical predictions based on  $\Lambda$ CDM models. The distance-independent distributions of their mass and color suggest that the group could have recently accreted new massive members from the surrounding fields. The systematically bluer colors of the brighter members indicate younger stellar population and higher star formation activities in them, which appears to be consistent with similar findings from the SAGA or ELVES survey. We suggest that the massive and bluer dwarf galaxies in the group have experienced less environmental quenching due to their recent accretion, while environmental quenching is more effective for the low-mass members. The interpretation of NGC 2997 being populationally young with recent accretion of massive members is also consistent with the overall morphological distribution of the dwarf galaxies showing a lack of morphologically evolved candidates but a plethora of irregularly shaped ones. Our detection rate of dwarf galaxy candidates in the NGC 2997 group and their inferred star formation activities are comparable to those found in Milky Way analog systems from recent surveys within the magnitude limit  $M_V \lesssim -13$  mag.

**Key words:** galaxies: dwarf — galaxies: individual (NGC 2997)

## 1 INTRODUCTION

The study of dwarf galaxies plays a crucial role in our understanding of several important issues in astronomy. It provides critical insights into the processes through which galaxy formation/evolution occurs, as well as observational tests for the distribution of dark matter and the  $\Lambda$ CDM model. For example, studies of dwarf galaxies based on large surveys have shown that satellite galaxies form in more than one channel (e.g. Lisker et al. 2007), and dwarf galaxies appear to show an extreme range in the amount of dark matter content, from being almost free of dark matter to being almost entirely made of dark matter (e.g. van Dokkum et al. 2016; Khalifeh & Jimenez 2021). Despite recent efforts, there exists a substantial gap in our understanding of the origin and properties of dwarf galaxies, such as the well-known discrepancies in central densities and abundance of dwarf galaxies between observational data on the Milky Way system and the  $\Lambda$ CDM model predictions, known as the “small-scale challenges” (Weinberg et al. 2015; Mao et al. 2021), or whether “galactic conformity” is universal in which both central host galaxies and satellite galaxies show similar properties in star-formation or colors (Weinmann et al. 2006; Otter et al. 2020; Poulain et al. 2021).

The availability of recent wide-field deep survey data has made it possible to study dwarf galaxies and their properties beyond the Milky Way (MW) and the Local Group ( $\lesssim 3$  Mpc; Redd 2018), furthering our understanding of their luminosity functions (LFs) and star formation activities in nearby groups. Dwarf galaxies identified in the fields of M81 (at 3.6 Mpc; Chiboucas et al. 2009), NGC 5128 (at 3.8 Mpc; Crnojević et al. 2016), M83 (at 4.0 Mpc; Müller et al. 2015), M101 (at 7.0 Mpc; Bennet et al. 2019), NGC 2784 (at 9.8 Mpc; Park et al. 2017), M96 (at 10.7 Mpc; Müller et al. 2018), and NGC 3585 (at 20.4 Mpc; Park et al. 2019) have extended LFs of dwarf satellites down to  $M_V \approx -7$  mag, showing discrepancies that the observed faint-end slopes are still consistently flatter than the  $\Lambda$ CDM model predictions (e.g., Klypin et al. 1999; Trentham & Tully 2002; Springel et al. 2008; Han et al. 2016; Li et al. 2019). The recent SAGA survey (Geha et al. 2017; Mao et al. 2021), ELVES survey (Carlsten et al. 2021b, 2022), as well as studies of nearby groups such as M101 (Bennet et al. 2019) and M94 (Bennet et al. 2020), on the other hand, have shown that star formation in the faint ( $M_V \gtrsim -12$  mag) satellite galaxies of MW-analog systems at  $\lesssim 41$  Mpc is significantly less active than the massive ones, providing

opportunities to understand the effects of mass and environment on quenching processes (e.g., Samuel et al. 2022). In addition, some studies have revealed the presence of apparent magnitude “gaps” or “humps” in some of the observed LFs: the former wherein no galaxies found (e.g., Bennet et al. 2019), while the latter with sudden increase of the LF slopes (e.g., Park et al. 2019). They also show a morphological diversity in dwarf galaxies, ranging from ultra-diffuse galaxies (UDGs) to nucleated dwarf galaxies (e.g., van Dokkum et al. 2015; Park et al. 2017; Müller et al. 2018; Bennet et al. 2019; Park et al. 2019). The origin of these features may bear important clues to our understanding of gravitational interactions among the members and the host of a galaxy group as well as the environmental effects to their evolutionary paths.

We have recently begun a systematic search of dwarf galaxies around more than 100 nearby galaxies observable in the Southern Hemisphere using deep stacked images from the Korea Microlensing Telescope Network (KMTNet, Kim et al. 2016) Supernova Program (KSP, Moon et al. 2016). By stacking several hundred, sometimes exceeding 1000, 60-s *BVI* images obtained with the three wide-field ( $= 2^\circ \times 2^\circ$  at a pixel sampling of  $0''.4$  per pixel) 1.6-meter telescopes located in Chile, South Africa and Australia that are primarily dedicated to detecting supernovae and optical transients during their early phases (e.g., Afsariardchi et al. 2019; Moon et al. 2021; Lee et al. 2022; Ni et al. 2022, 2023a,b), we expect to discover a substantial number of new dwarf galaxies on images that readily reach a limiting surface brightness of  $\gtrsim 28$  mag arcsec $^{-2}$ . In our previous two studies of the NGC 2784 and NGC 3585 groups using the KSP data, we reported discoveries of 30 (for NGC 2784) and 46 (NGC 3585) new dwarf galaxies (Park et al. 2017; Park et al. 2019). One particular advantage of the KSP-data based studies of dwarf galaxies is the homogeneity of data obtained with three colors of *BVI*, which can enable unprecedented systematic comparative studies and statistical analyses of the discovered dwarf galaxies in different groups/clusters. This can potentially lead to in-depth understanding of how different types of host galaxies and environments influence differently to the evolution of satellite galaxies in their structural, morphological and dynamical features.

In this paper, we present our KSP based discoveries of dwarf galaxies in the field of NGC 2997, which are our first dwarf galaxy discoveries around a spiral-type host galaxy using the KSP data. NGC 2997 is a giant spiral galaxy of type SAB(rs)c with a redshift of  $z \approx 0.003611$  (Meyer et al. 2004) and an inclination angle of  $40^\circ$  (Milliard & Marcelin 1981). It is the largest member of the loose galaxy group LGG 180 (Garcia 1993) and is relatively isolated from other major galaxies with no known companion within  $\sim 110$  kpc (Hess et al. 2009). The galaxy is reported to have a dynamical mass of  $2.1 \times 10^{11} M_\odot$ , a gas accretion rate of  $1.2 M_\odot \text{ yr}^{-1}$ , and a thick H I disk (Hess et al. 2009). It has an *I*-band apparent magnitude of  $I \approx 9.88$  mag (Doyle et al. 2005), and a *K*-band apparent magnitude of  $K \approx 6.41$  mag (Skrutskie et al. 2006). The distance to NGC 2997 has been estimated to be in the range of 9.5–14.8 Mpc, including: (1) 9.5 Mpc using tertiary distance indicators (magnitudes, luminosity index, and diameters) (de Vaucouleurs 1979; Larsen & Richtler 1999), (2) 14.8 Mpc from the multi-attractor velocity flow model (Masters 2005) with  $H_0 = 72 \text{ km s}^{-1} \text{ Mpc}^{-1}$  (Pisano et al. 2011), and (3)  $12.2 \pm 0.9$  Mpc based on the near-infrared Tully-Fisher relation (Hess et al. 2009). We adopt the distance of 12.2 Mpc from Hess et al. (2009) in this work. Its absolute *K*-band magnitude is  $-24.02$  mag, which is within the range of  $-23$  to  $-24.4$  mag of the MW-analog galaxies studied in the SAGA (Geha et al. 2017; Mao et al. 2021) or ELVES survey (Carlsten et al. 2021b, 2022). Hence, this provides an opportunity of comparing dwarf galaxies identified

in another MW-analog host at a closer distance with much deeper limiting magnitudes than those in the SAGA survey at  $> 25$  Mpc. In §2, we provide the details of our observations and data reduction process, while we describe the identification of dwarf galaxy candidates (DGCs) and how we measure their photometric and morphological properties in §3. §4 details group properties of the DGCs, including their radial distributions, color and structural parameters, and luminosity function. We discuss in §5 that the observed features of the NGC 2997 group are compatible with a scenario that the group has recently been accreting massive, blue dwarf galaxies from the surrounding fields. We summarize our conclusions in §6.

## 2 OBSERVATIONS AND DATA REDUCTION

As part of the KSP (see above), we had monitored two  $4 \square^\circ$  fields around the giant spiral galaxy NGC 2997 between February 2017 and June 2019. The wide field ( $= 2^\circ \times 2^\circ$ ) CCD cameras of the KMTNet consist of four E2V CCD chips, with each chip covering  $1 \square^\circ$  field at a sampling size of  $0''.4$  per pixel. There is a gap of  $3:1$  between the chips in the east-west direction, while that in the north-south direction is  $6:2$ . Figure 1 shows the distribution of the two observed fields in *I*-band, composed of eight sub-fields of  $1 \square^\circ$ , with two sub-fields largely overlapping near the center of the entire field, where the host galaxy NGC 2997 is located. The four sub-fields in the north-west of the image belong to the first field (F1) observed mostly between February 2017 and January 2018, while those in the south-east belong to the second field (F2) observed between February 2018 and June 2019. As a result, the effective size of the field that we observed for NGC 2997 is about  $7 \square^\circ$ , with the  $1 \square^\circ$  sub-field directly surrounding the central galaxy observed almost  $2\times$  longer than the other sub-fields. We stack 682, 716, and 798 individual frames of 60-second exposures whose seeing is better than  $2''$  to create the deep stacked images for F1 in the *BVI*-bands using SWARP (Bertin et al. 2002). For F2, we stack 761 (*B*), 810 (*V*), and 880 (*I*) frames. The final seeing in the stacked images is in the range of  $1''.3$ – $1''.6$  for the *BVI*-bands of all eight sub-fields, as shown in Table 1. The average point source  $3\text{-}\sigma$  limiting magnitudes in the stacked images of the first field are  $B = 25.14 \pm 0.18$  mag,  $V = 24.69 \pm 0.24$  mag, and  $I = 24.40 \pm 0.36$  mag, while those of the second field are  $B = 25.16 \pm 0.24$  mag,  $V = 24.79 \pm 0.31$  mag and  $I = 24.51 \pm 0.36$  mag.

We carry out photometric calibration of KMTNet CCD images using standard reference stars from the AAVSO Photometric All-Sky Survey (APASS)<sup>1</sup> catalog that are in our fields, and the SuperNova Analysis Package (SNAP)<sup>2</sup>. In order to secure high signal-to-noise (S/N) ratios while avoiding CCD saturation and non-linearity effects, only the reference stars whose apparent magnitudes are in the range of 15–17 mag are used in the calibration. The APASS photometric system is based on the standard Johnson *BV* and the Sloan *i* filter bands. It has been known that the calibration of KMTNet instrumental magnitudes against the Johnson *B*-band magnitudes requires a color correction of  $\approx 0.27 \times (B - V)$  (see Park et al. 2017, for details). After confirming the presence of the same color dependence in our images, we made the same color corrections on *B*-band magnitudes of the DGCs. No such color dependency or offset has been identified for the *V*-band. Although no color dependency exists between the Sloan *i*-band and the KMTNet *I*-band, a 0.4 mag offset is found between them from the comparison of the Landolt and OGLE standard stars

<sup>1</sup> <https://www.aavso.org/apass>

<sup>2</sup> <https://github.com/niyuanqi/SNAP>

**Table 1.** Seeing of the stacked images for the eight sub-fields

Sub-field	<i>B</i> (arcsecs)	<i>V</i> (arcsecs)	<i>I</i> (arcsecs)
NGC2997-F1-Q0	1.57±0.07	1.44±0.05	1.36±0.04
NGC2997-F1-Q1	1.53±0.06	1.43±0.05	1.34±0.04
NGC2997-F1-Q2	1.52±0.06	1.42±0.04	1.35±0.04
NGC2997-F1-Q3	1.48±0.04	1.40±0.04	1.34±0.04
NGC2997-F2-Q0	1.60±0.06	1.47±0.06	1.36±0.05
NGC2997-F2-Q1	1.55±0.06	1.44±0.05	1.34±0.05
NGC2997-F2-Q2	1.58±0.04	1.46±0.04	1.37±0.04
NGC2997-F2-Q3	1.52±0.04	1.42±0.03	1.34±0.06

† F1 and F2 indicate the two observed fields, and Q0 to Q3 indicate the 4 sub-fields in each field.

**Table 2.** Zero-Point Instrumental Magnitude Offsets

Sub-field	<i>B</i>	<i>V</i>	<i>I</i>
NGC2997-F1-Q0	28.23	28.01	28.44
NGC2997-F1-Q1	28.30	28.00	28.41
NGC2997-F1-Q2	28.23	28.09	28.39
NGC2997-F1-Q3	28.29	28.05	28.37
NGC2997-F2-Q0	28.17	27.98	28.28
NGC2997-F2-Q1	28.22	27.93	28.39
NGC2997-F2-Q2	28.21	28.03	28.32
NGC2997-F2-Q3	28.23	28.00	28.35

† The 1- $\sigma$  uncertainties are 0.01 mag for all the sub-fields and filters.

**Table 3.** Previously Discovered Dwarf Galaxies and Their Properties

Name	<i>B</i> -band Magnitudes <sup>a</sup>	Redshift ( <i>z</i> )
ESO 434-33	13.19, 13.09	0.0032
ESO 434-27	15.22, 15.16	0.0031
LEDA 718707	17.24, 17.02	0.0034
ESO 434-39	15.55, 15.38	0.0034
ESO 434-34	14.06, 14.24	0.0033
IC 2507	13.12, 12.93	0.0042
ESO 434-41	14.69, 14.60	0.0033

<sup>a</sup>The previously measured magnitudes and the magnitudes obtained in this study (see the text).

(Park et al. 2017, see §3.4 therein, and also Kim et al. in preparation). We, therefore, adopt 0.4 magnitude difference between the KMTNet *I*-band and APASS *i*-band photometry:  $I = i - 0.4$  mag. Table 2 contains the zero-point magnitude offsets of our images. According to the Galactic extinction model of Schlafly & Finkbeiner (2011)<sup>3</sup>, the Galactic extinction in the direction of NGC 2997 are  $A_B = 0.392$ ,  $A_V = 0.296$ , and  $A_I = 0.163$  mag. All the magnitudes that we provide in this study are corrected with these extinction values.

<sup>3</sup> <https://ned.ipac.caltech.edu/>

### 3 DWARF GALAXY CANDIDATES AND BASIC PROPERTIES

#### 3.1 Search of Dwarf Galaxy Candidates

We conduct a thorough visual inspection on stacked KMTNet images of the eight sub-fields to identify DGCs around NGC 2997. We use the *I*-band images in this search of DGCs, applying the selection criteria of being a diffuse source extending more than 20 pixels (or  $\approx 8''$ ) that is absent of any prominent structures (e.g., spirals or bars), except for potential nucleated centers, as was done in Park et al. (2017) and Park et al. (2019) for the NGC 2784 and NGC 3585 fields, respectively. Four<sup>4</sup> inspectors individually inspected the images and made a list of candidates of their own. 44 dwarf galaxy candidates were co-selected by all four members in their independent identification, and 11 more are additionally added unanimously after a second round of examination on candidates that were originally selected by less than 4 inspectors. In addition to the *I*-band images, the *B*- and *V*-band images are also used to confirm the identified DGCs. As a result, we identify 55 DGCs in total, with 80% of them being selected in the first round. Figure 1 shows their locations around NGC 2997 on the stacked *I*-band image. We note that there are more DGCs in the south-eastern part of NGC 2997 than in the north-western part, especially in the region  $\gtrsim 1.3^\circ$  away from the galaxy where there are twice as much DGCs in the south-eastern corner. Figure 2 shows example cutout images of 8 DGCs, while the images of all 55 DGCs is available in the appendix (Figure A1).

Out of the 55 DGCs, seven were previously identified in the ESO and LEDA catalogs (Lauberts & Valentijn 1989; Paturel et al. 2003). Five of these (i.e., ESO 434-27, ESO 434-31 [= IC 2507], ESO 434-33, ESO 434-34 and ESO 434-41) are known to be members of the loose galaxy group LGG 180 in which NGC 2997 is the largest member (Garcia 1993). The redshifts of the other two (i.e., ESO 434-39 and LEDA 718707) are similar to that of NGC 2997 (Jones et al. 2009). Although we recovered three other dwarf galaxies (i.e., ESO 434-30, ESO 434-43, and LEDA 100726) that were previously presented in the catalogs, we exclude them from our final list because their redshifts are significantly larger than  $z \approx 0.0036$  of NGC 2997: 0.0071 (ESO 434-30; Meyer et al. 2004), 0.0083 (ESO 434-43; Theureau et al. 1998), and 0.0080 (LEDA 100726; Matthews et al. 1995). Table 3 shows redshifts of the seven previously discovered dwarf galaxies.

The two fields that we observed towards NGC 2997 are slightly different in the total number of stacked images because the second field has about 10 % more images and is therefore deeper than the first by  $\lesssim 0.1$  mag (Table 2). The photometric depth difference is at the level of the photometric uncertainties of the two fields, indicating that the difference in depth is not significant. This conclusion is supported by our identification of the exact same number of DGCs in the overlapping sub-fields between the first and second field: NGC2997-F1-Q2 and NGC2997-F2-Q1. We conduct a completeness test of our dwarf galaxy identification on the stacked *I*-band images by inserting 600 artificial galaxies created with the following seven parameters: position angle, ellipticity, Sérsic index, *I*-band magnitude, effective radius, effective surface brightness, and central surface brightness. The position angles and ellipticity of them are random distributions between  $-90$  and  $90$  degrees and 0.05 and 0.9, respectively, while Sérsic indices are between 0.1 and 1., which contain most of common cases (e.g., see bottom panel of Figure 10). We conduct a random sampling of the *I*-band magnitudes in the range of 11.3–21.7 mag,

<sup>4</sup> TJF, HSP, YDL and SCK from the author list

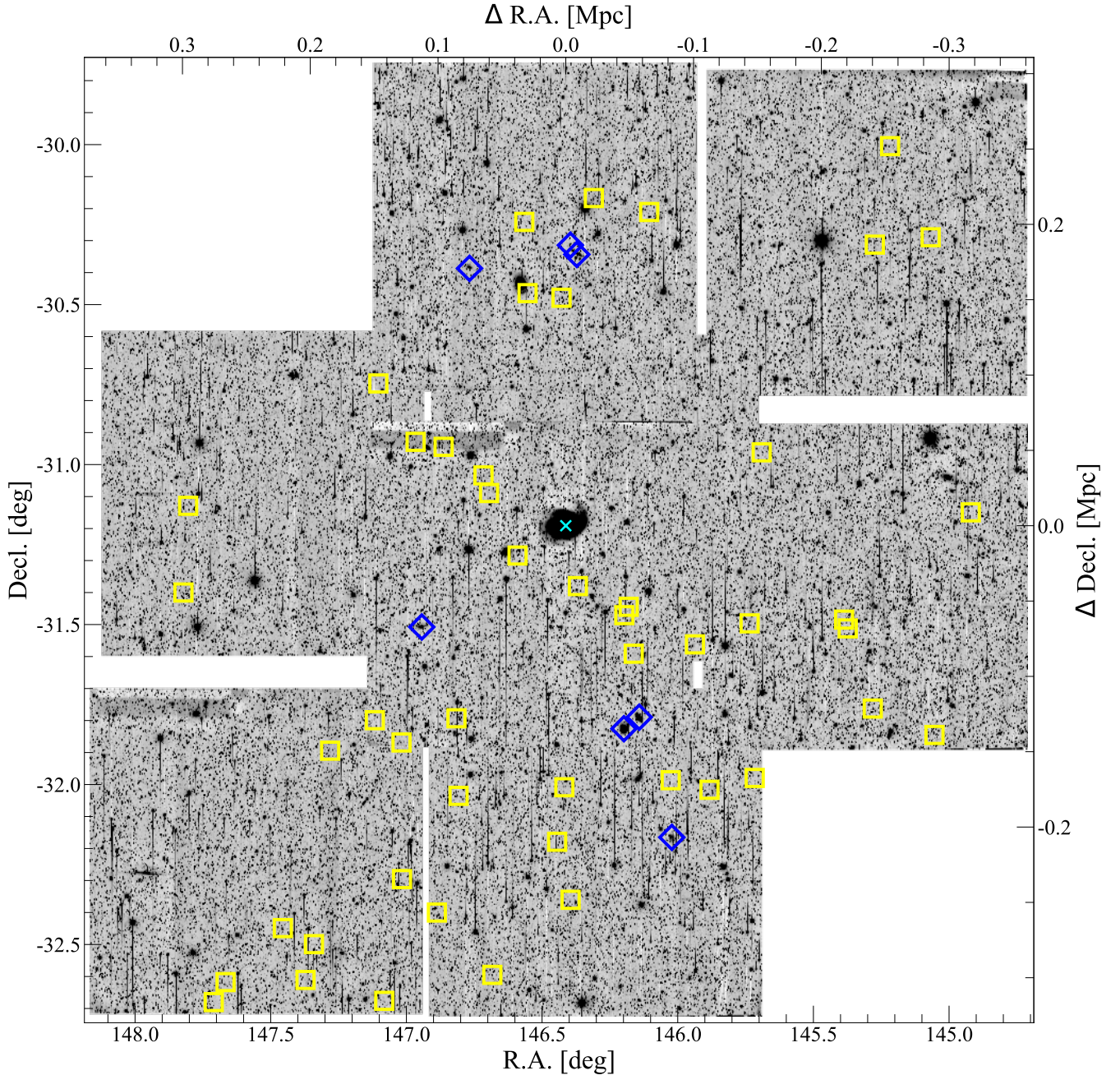


**Figure 1.** *I*-band stacked KMTNet images of about  $7\text{ deg}^2$  around the galaxy NGC 2997 (cyan cross at the center). The blue open diamonds mark the locations of 7 previously discovered dwarf galaxies (See § 3.1). The yellow open squares mark the other 48 DGCs.

which is 1 mag broader than the magnitude range of the 55 DGCs in order to include dwarf galaxies that might be outside of our detection limits. For the effective radius, effective surface brightness, and central brightness of the artificial galaxies, we construct their Gaussian random distributions centered at the values expected from the linear relations between them and the *I*-band magnitudes obtained from the 55 DGCs in our sample. The Gaussian RMS widths of these distributions are equivalent to 1.6 times the dispersion of the parameters obtained from the 55 DGCs, which effectively expands volume of the parameter space for the artificial galaxies. We find a 90% completeness level down to  $I \approx 19.0$  mag (or  $M_V \approx -10.6$  mag

at the distance of NGC 2997) and  $\mu_{e,I} \approx 25.5$  mag arcsec $^{-2}$ . Our detection rate of bright DGCs in NGC 2997 is comparable with that of the SAGA survey (Mao et al. 2021) on 36 MW-analog galaxies. For example, in NGC 6181, a spiral galaxy with a mass similar to that of NGC 2997, the SAGA survey spectroscopically confirmed 9 satellites with  $M_V \lesssim -13$  mag. Adopting the same satellite selection criteria of SAGA — which are within the projected distance of  $\sim 300$  kpc and radial velocity  $\pm 275$  km s $^{-1}$  from the host — for the 10 DGCs with  $M_V \lesssim -13$  mag in our sample, we find that 7 of them can be confirmed as satellites. These 7 DGCs are the bright ones that were previously discovered (See Table 3). Since we do not

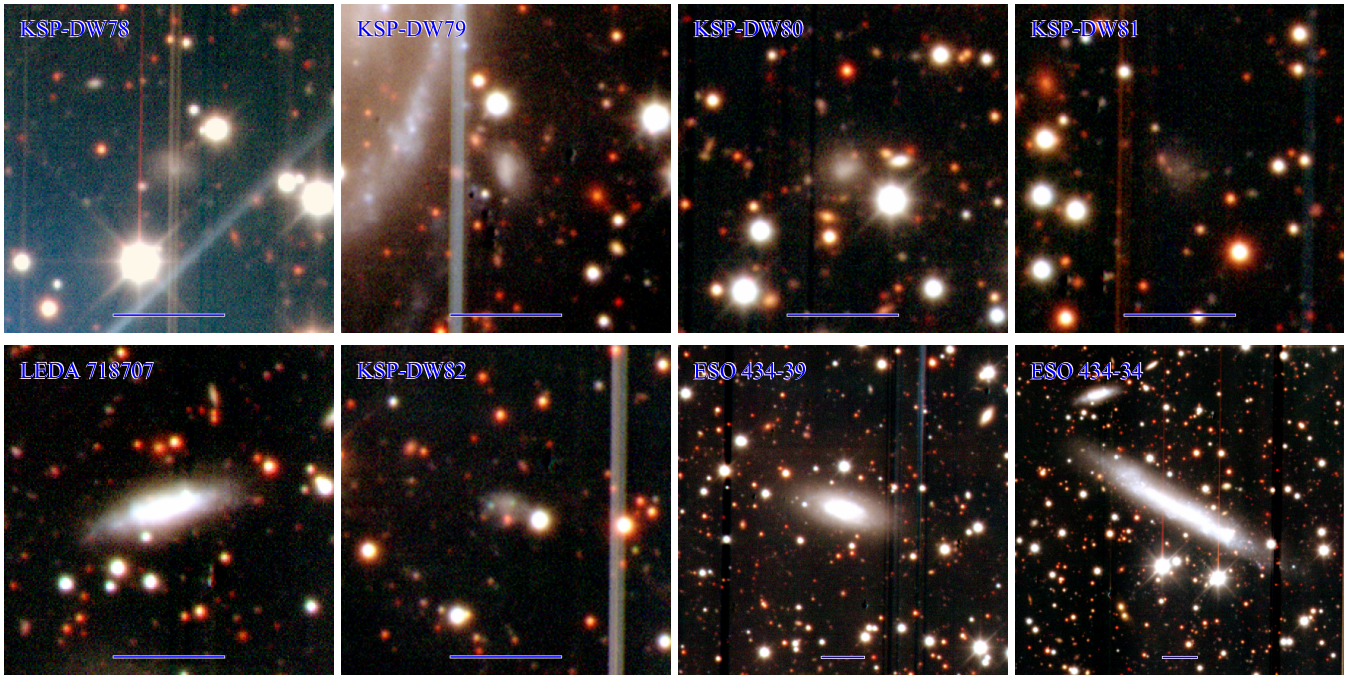


**Figure 2.** Example RGB cutout images of 8 (out of 55) DGCs in NGC 2997. North is up and east is to the left. The blue horizontal bar at the bottom of each image corresponds to an angular size of  $0'.5$  ( $= 1.77$  kpc at the distance of 12.2 Mpc). The cutout images of all 55 DGCs are available in Appendix (Figure A1).

have spectroscopic information for the remaining three DGCs, the number of confirmed satellites for NGC 2997 upon the same SAGA selection criteria is in the range of 7–10 in our study, comparable to 9 for NGC 6181 from SAGA.

The number density of contaminating background galaxies in typical KMTNet stacked images was estimated to be  $1.75 \pm 0.66 \text{ deg}^{-2}$  from the analysis of the KSP images of KK 196 field (Park et al. 2019), which has been observed in very similar manner to other KSP fields like NGC 3585 or NGC 2997. The distance to the KK 196 field, which belongs to the Centaurus A group, is only  $\sim 4$  Mpc, and dwarf galaxies belong to this group should appear resolved. Applying the same visual inspection procedures adopted for the KSP stacked images of NGC 2784 and NGC 3585 fields, Park et al. (2019) identified 11 dwarf galaxy candidates from the  $4 \text{ deg}^2$  KK 196 field. Out of these 11 identified dwarf galaxy candidates, 4 of them are resolved, while the rest 7 are unresolved. The 4 resolved candidates include 2 previously known dwarf galaxies associated with the Centaurus group. The 7 unresolved candidates appear to be randomly distributed in the field. Park et al. (2019) concluded that the 4 resolved candidates are associated with the Centaurus group, whereas the 7 unresolved candidates are unassociated with the group and, therefore, marked as background sources. This gives the contamination level of  $1.75 \pm 0.66 \text{ deg}^{-2}$  for the stacked KSP images of KK 196 field. Assuming the same background contamination level between the KK 196 and NGC 2997 field images that have very similar photometric depths, we estimate 7–16 as the number of potential background contamination sources for the 55 DGCs in the NGC 2997 group.

We note that our background contamination estimation based on Park et al. (2019) has not included the possibility that contamination could be dependent on the observed properties of the DGCs. Results from the ELVES survey (Carlsten et al. 2021a) have shown that the background contamination rate is dependent on the luminosity and central surface brightness of dwarf galaxies, such that the contaminants tend to be fainter overall but have a larger central

surface brightness, and the number of contaminants in the ELVES survey starts to increase substantially for  $M_V \gtrsim -13$ . This is more or less similar to the findings from Park et al. (2019) that show all the contaminants are fainter than  $M_V = -12.5$  mag at the distance of NGC 2997, indicating that the 7–16 potential contaminants in the field are more likely to have  $M_V \gtrsim -12.5$  mag with larger central surface brightness. Due to our visual identification procedure of DGCs (§ 3.1), they are less likely background early-type ellipticals, which have steep surface brightness profiles from the center, and are more likely blue, luminous late-type galaxies in the background.

### 3.2 Surface Photometry and Catalog

We carry out surface photometry of the 55 DGCs by constructing their radial isophotal profiles using the *ELLIPSE* fitting task from the python-based photometry package *Photutils*<sup>5</sup>. The *ELLIPSE* task calculates the best-fit isophotal parameters (i.e., the central position, positional angle, and ellipticity) by fitting a galaxy based on the initial visual estimations of those parameters under the assumption of an elliptical geometry. The typical linear step-size of fitting is 2–3 pixels along the semi-major axis; however, for the brighter and larger ( $r_e > 15''$ ) sources, we conduct the fitting in logarithmic scale for efficiency. We mask out foreground/background objects that overlap with the DGCs when possible. The intensity of each isophote is determined by the median value of the isophote’s pixels, which effectively minimizes the influence of any interfering artifacts/sources in the foreground/background; and the total intensity of each isophote is obtained by multiplying the median value with the total number of pixels within. The sky background level, which is estimated using the median value of source-free pixels surrounding a DGC, is subtracted from the isophotal intensities. The outermost isophote of

<sup>5</sup> <https://photutils.readthedocs.io/en/stable/>

a DGC is determined when the isophotal intensity is  $\approx 1\text{-}\sigma$  above the sky background level. We then estimate the total instrumental magnitudes of the DGCs by integrating the total intensities of their isophotal models. Figure 3 shows example results for 6 dwarf galaxy candidates where the data, masked data, models, and residuals are shown. For the  $B$ - and  $V$ -band images of the DGCs, we follow the same procedure above using the isophotal models from  $I$ -band images to construct their surface brightness profiles as well as their instrumental magnitudes in  $B$ - and  $V$ -bands. Finally, we obtain the corrected apparent magnitudes of the DGCs as outlined in §2, including the conversion from instrumental magnitudes to apparent magnitudes using zero-point offsets (Table 2),  $B$ -band color correction and  $I$ -band magnitude offset correction, as well as Galactic extinction correction.

We investigate the effective performance of our isophotal photometry by comparing the isophotal model magnitudes of 13 relatively isolated DGCs in our sample with their magnitudes obtained by direct aperture photometry. The 13 DGCs are the entirety of DGCs that appear to be free from apparently significant interference by overlapping sources. The magnitude differences between the two methods are small, with 75% of them showing differences  $\lesssim 0.05$  mag, although a few of them reach differences of  $\sim 0.2$  mag. We note that the isophotal method produces slightly larger (= fainter) magnitudes than the aperture photometry method. One possible explanation for this is the contribution by faint overlapping sources to the aperture photometry. The 7 previously-discovered dwarf galaxies in Table 3, for which  $B$ -band magnitudes from previous studies are available, do not belong to this group of 13 apparently isolated DGCs. The average  $B$ -band magnitude differences between their literature values and isophotal model magnitudes obtained in this study is 0.14 mag. We, therefore, conclude that there exists a reasonable agreement between magnitudes obtained by our isophotal method and aperture photometry method, as well as those obtained in previous studies.

All the DGCs in our sample have  $r_e \geq 2''.39$ , which is greater than the seeing of our stacked images in the range of  $1''.3\text{--}1''.6$  (Table 1), and the PSF effects to our photometry of the DGCs are expected to be small. We examine the PSF effects to our photometry of eight (= DW-93, 104, 88, 102, 115, 101, 120, 118) smallest DGCs in our sample with  $r_e < 4''$  given that the PSF effects can be more apparent for small DGCs. First, the differences between the total  $BVI$  magnitudes obtained by our isophotal models and by PSF convoluted models of these eight DGCs are very small, with most of them being  $\leq 0.01$  magnitudes. We also find that the average differences of their estimated effective radius, effective brightness, and Sérsic index between the two methods are  $0''.15$ ,  $0''.07$  mag arcsec $^{-2}$ , and 0.03, respectively. These values are much smaller than their propagated measurement uncertainties of  $0''.94$ ,  $0.52$  mag arcsec $^{-2}$ , and 0.2, respectively, based on their uncertainties in Table 4. We therefore conclude that the PSF effect on our galaxy parameters estimation is not significant.

Figure 4 shows eight examples of surface brightness profiles obtained from our surface photometry (full figure in appendix, Figure A2). The top panels show the  $I$ -band surface brightness profiles (black crosses) that we obtained using median values of their isophotes for the 55 DGCs. To examine the radial distributions of light, we fit the surface brightness profiles with the Sérsic function  $\mu_I = \mu_{o,I} + 1.0857 (r/r_{o,I})^{1/n_I}$ , where  $\mu_I$ ,  $\mu_{o,I}$ ,  $r$ ,  $r_{o,I}$  and  $n_I$  are the surface brightness, central surface brightness, radius, scale length, and Sérsic index. During the fitting, we only use isophotes with intensities higher than the sky background level at a confidence level of 90% ( $1.6\text{-}\sigma$ ), and those isophotes used in the fitting are marked by red circles in Figure 4. The solid blue curves in the figure

represent the best-fit Sérsic profiles, and the vertical dashed lines in blue indicate the effective radius  $r_e = (2.3026 \times Bn)^n r_o$ , where  $Bn = 0.868n - 0.142$  (Chiboucas et al. 2009). The orange dotted curves in 8 of the surface brightness profiles are the PSF models of the images to which the corresponding DGCs belong. The bottom panels show the DGCs' color profiles — green open circles for  $(B - V)_0$  and black crosses for  $(V - I)_0$ . The green and red dashed lines indicate the values for  $(B - V)_0$  and  $(V - I)_0$  colors obtained using the difference in total magnitudes, respectively. Table 4 lists the parameters of the 55 DGCs including their names, coordinates,  $I$ -band total apparent magnitudes ( $I$ ),  $(V - I)_0$  and  $(B - V)_0$  colors, three best-fit Sérsic parameters (i.e.,  $\mu_{o,I}$ ,  $r_{o,I}$ ,  $n_I$ ), effective radius in  $I$ -band ( $r_{e,I}$ ), and  $V$ -band total absolute magnitudes ( $M_V$ ). The final column (“Comments”) shows if the candidates are morphologically identified as ultra-diffuse, or nucleated, or irregular galaxies (see § 3.3). All the DGCs are brighter than 21.24 mag in  $I$ -band, whereas the faintest  $B$ -band and  $V$ -band magnitudes are 23.98 and 22.41 mag, respectively. Their colors are in the range of 0.39 – 1.17 mag for  $(V - I)_0$ , and 0.25 – 1.57 mag for  $(B - V)_0$ . The central surface brightnesses of all candidates are brighter than  $\mu_{o,B} \approx 27.9$ ,  $\mu_{o,V} \approx 26.7$ , and  $\mu_{o,I} \approx 25.4$  mag arcsec $^{-2}$ . The  $I$ -band Sérsic scale lengths and the curvature indices vary in the range of  $2''.5 \lesssim r_{o,I} \lesssim 57''.9$  and  $0.25 \lesssim n_I \lesssim 1.39$ , respectively. The  $I$ -band effective radii ( $r_{e,I}$ ) are in the range of  $2''.4\text{--}50''.4$ , or 0.142–2.97 kpc at the distance of 12.2 Mpc. About 87% (or 48 out of 55) have effective radii smaller than  $12''$  (or 0.71 kpc). The largest newly discovered DGC in our sample is KSP-DW106, a very elongated source with an  $I$ -band effective radius of  $22''.9$ . However, it is smaller than most of the 7 previously discovered candidates.

### 3.3 Morphological Classifications: Nucleated, Ultra-Diffuse, and Irregular Dwarf Galaxies

Dwarf galaxies with distinctively bright and compact cores have been morphologically classified as nucleated dwarf galaxies (e.g., Côté et al. 2006; Trentham & Tully 2009; Park et al. 2019; Zaritsky et al. 2021). We identify KSP-DW91 to be the only nucleated dwarf galaxy out of the 55 DGCs in NGC 2997 based on the presence of a clearly distinguishable central point-source core with color similar to the rest of the galaxy (Figure A1), although 0.22 mag arcsec $^{-2}$  difference of the core in the  $V$ -band from the Sérsic-fit expected brightness is a bit smaller than those found in nucleated dwarf galaxies in other groups (e.g., Park et al. 2019). The lack of nucleated dwarf galaxies in NGC 2997 is in stark contrast with the range of 10–30 % of the incidence rate from previous studies (e.g., Trentham & Tully 2009; Park et al. 2017; Park et al. 2019).

Dwarf galaxies with extremely diffuse morphological features have been classified as ultra-diffuse galaxies (UDGs; e.g., van Dokkum et al. 2015; Müller et al. 2018; Park et al. 2019). For example, van Dokkum et al. (2015) applies the following criteria to identify UDGs:  $\mu_{o,V} \geq 23.7$  mag arcsec $^{-2}$  and  $r_{e,V} \geq 1.5$  kpc. The two DGCs with the most extreme diffuse distribution of surface brightness in our sample are KSP-DW106 ( $r_{e,V} = 1.38 \pm 0.4$  kpc,  $\mu_{o,V} = 25.23 \pm 0.11$  mag arcsec $^{-2}$ ) and KSP-DW107 ( $r_{e,V} = 0.66 \pm 0.48$  kpc,  $\mu_{o,V} = 25.78 \pm 0.17$  mag arcsec $^{-2}$ ). If we apply the same criteria above, KSP-DW106 can be classified as a potential UDG, given its effective radius uncertainty.

Finally, we identify 17 DGCs irregularly-shaped dwarf galaxies in our sample based on the presence of clearly non-elliptical morphology, faint but still identifiable structures, or the peak emission being off the geometrical center. Their average values of effective radius ( $I$ -band), absolute magnitudes ( $V$ -band), and  $(B - V)_0$  color are

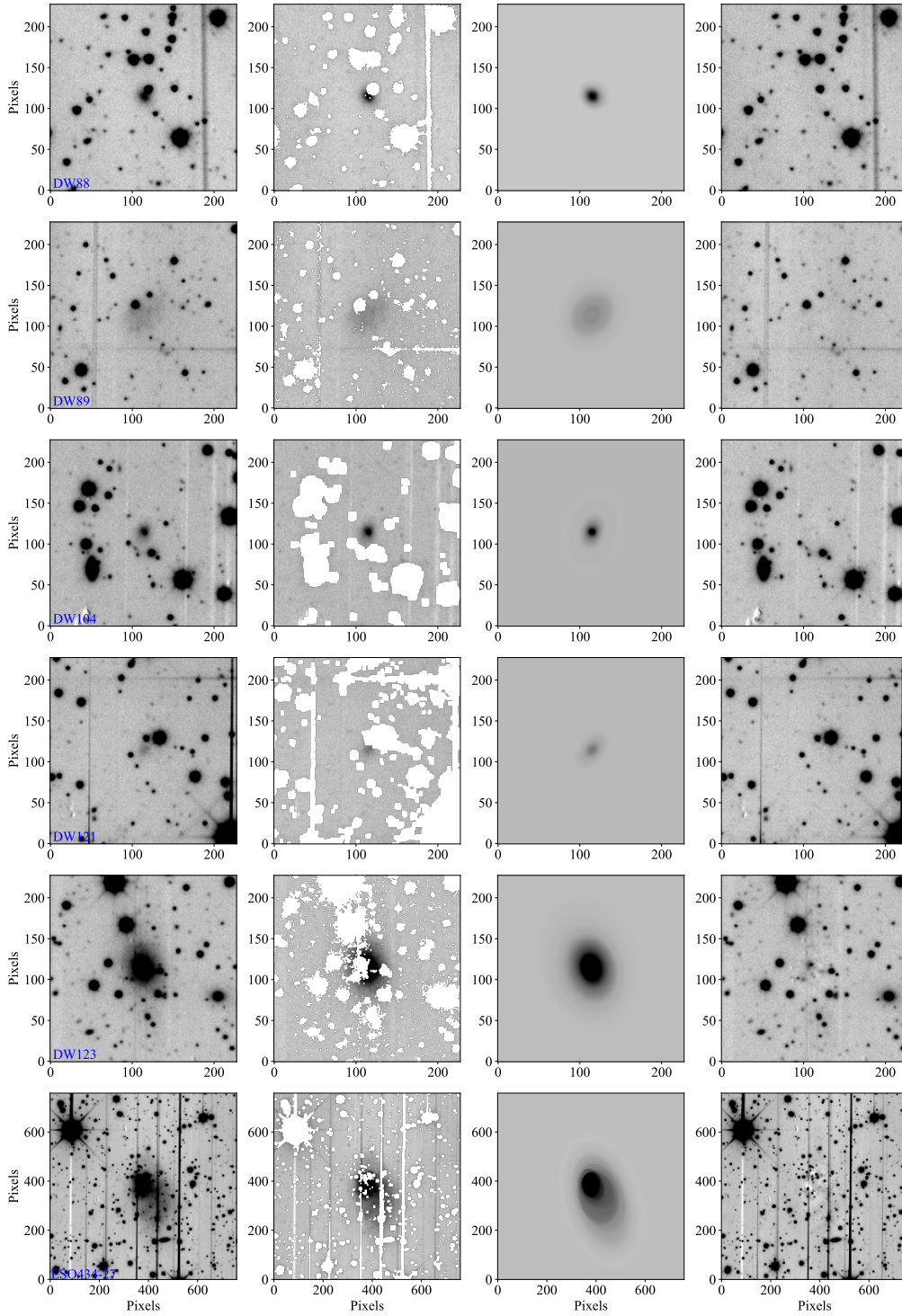


**Figure 3.** Cutout images of the six example DGCs demonstrating our photometric processes for obtaining isophotal models: DW88, DW89, DW104, DW121, DW123 and ESO434-27 from top to bottom. The rows are for the data (or stacked images; first row), the data with masks (second row), fitted isophotal models (third row), and residual of the data after subtraction of the isophotal models (see § 3.2).

$16''.07$  (or  $0.95$  kpc),  $-13.56$  mag, and  $0.47$  mag, respectively. These irregularly-shaped dwarf galaxies, which include all the 7 previously discovered dwarf galaxies (Table 4), appear to be significantly larger, brighter, and bluer than  $r_{e,I} \approx 8''.80$  (or  $0.52$  kpc),  $M_V \approx -11.61$  mag, and  $(B - V)_0 \approx 0.60$  mag, which are the average values for the entire DGC population. We note that it is easier to select large

DGCs as irregular than smaller ones due to our selection criteria, and there could be a group of small irregularly-shaped DGCs that was not selected. The real difference in size, brightness and color between the irregularly-shaped DGCs and the entire DGC population of NGC 2997, therefore, could be smaller.

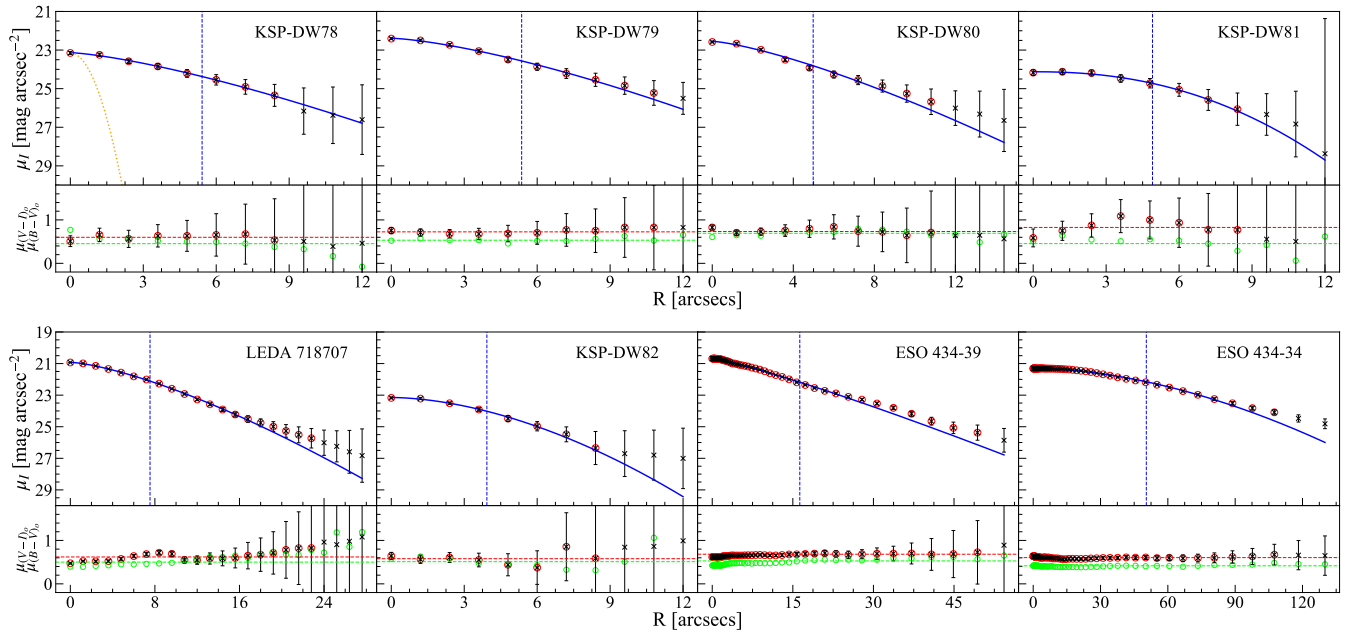


**Figure 4.** Eight examples of surface brightness profiles of the DGCs. *Upper Panels:*  $I$ -band surface brightness profiles. The black crosses with error bars, often encircled by a red circle, represent  $\mu_I$  and its uncertainty. Only those data points with a red circle are used in 1D Sérsic fitting. The blue solid curves show the resulting best-fit Sérsic profiles. The vertical blue dashed lines mark the estimated effective radii. *Lower Panels:*  $(B - V)_0$  and  $(V - I)_0$  color profiles are shown in green circles and black crosses, respectively. The green and red horizontal dashed lines represent the mean  $(B - V)_0$  and  $(V - I)_0$  colors obtained from difference in total apparent magnitudes (See § 3.2), respectively. The dotted orange curve in the surface brightness profile of KSP-DW78 represents the PSF profile of the image to which the dwarf galaxy belongs. The surface brightness profiles of all 55 DGCs and the PSF profiles of all 8 images are available in Appendix (Figure A2).

#### 4 PROPERTIES OF DWARF GALAXY CANDIDATES IN THE NGC 2997 GROUP

##### 4.1 Radial Distribution of Number Density and Color

Figure 5 shows the projected radial number density distribution (filled circles) of DGCs in the NGC 2997 group decreasing with radial distance after subtracting the expected background contamination,  $1.75 \text{ DGCs deg}^{-2}$  (see §3.1). We adopt both linear and logarithmic radial distance binnings in panel a) and b), as was done in previous studies (Park et al. 2017; Park et al. 2019). We fit the exponential function  $\Sigma = e^{\alpha R + \beta}$ , where  $R$  is the projected distance, to the number density distribution, and we obtain the best-fit parameters  $\alpha = -1.03 \pm 0.40$  and  $\beta = 2.75 \pm 0.37$ , shown as the dashed line in panel a). In the fitting, we exclude the last data point from the outermost bin at  $R = 1.9^\circ$  to minimize the effects of the unexpected concentration of DGCs in the south-eastern corner of the field (see §3.1). The dashed line in panel b) represents the best-fit power-law function  $\Sigma = \alpha R^\beta$ , with  $\alpha = 5.23 \pm 1.03$  and  $\beta = -0.57 \pm 0.33$ .

Figure 6 compare the radial distributions of the binned number density (top panel) and mean  $(B - V)_0$  color (bottom panel) between bright and faint groups of DGCs in the NGC 2997 group divided by their median brightness of  $M_V = -11.02 \text{ mag}$ . The radial number density distributions of both groups — filled squares for the bright group and filled triangles for the faint group (top panel), are largely similar to each other, resulting in a relatively flat radial distribution of the fraction of bright galaxies (filled circles). The best-fit parameters of the exponential function ( $\Sigma = e^{\alpha R + \beta}$ ) for the radial number density distribution are  $\alpha = -0.83 \pm 0.54$  and  $\beta = 2.02 \pm 0.51$  (bright group) and  $\alpha = -0.86 \pm 0.52$  and  $\beta = 1.96 \pm 0.52$  (faint group). All the DGCs located at  $R > 1.6^\circ$  belong to the faint group, and the outermost data point is excluded from the fitting as above.

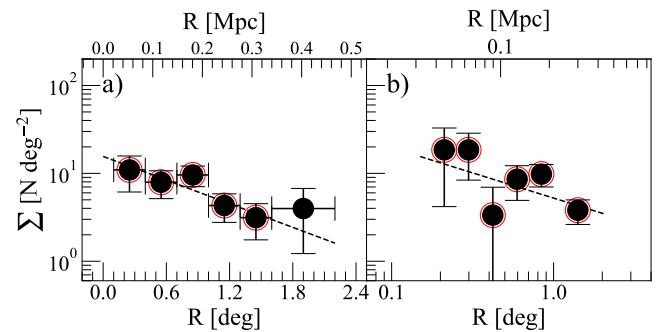


**Figure 5.** Radial number density profiles of the 55 DGCs in the NGC 2997 group in linear (left) and logarithmic (right) scale in x-axis. The dashed line in panel a) shows the best-fit exponential function for  $R \lesssim 1.6^\circ$  (see §4.1) obtained by fitting the first five data points, excluding the last one. The dashed line in panel b) shows the best-fit power-law function obtained using all the six data points in the panel.

The binned mean  $(B - V)_0$  color distributions of both groups — blue curve for the bright group and red curve for the faint group (bottom panel) — largely appear to be constant along the radial distance without any significant difference between them, resulting in a flat distribution of the mean  $(B - V)_0$  color for the 55 DGCs (filled black circles). The filled blue and red circles represent colors of all individual DGCs: blue for the DGCs of the bright group and red for the faint group. The three DGCs (KSP-DW85, KSP-DW94, and KSP-DW102) with exceptionally red colors  $(B - V)_0 \gtrsim 1.10 \text{ mag}$  (empty circles; Table 4) are very faint, i.e.,  $M_V \gtrsim -10.35 \text{ mag}$ , and apparently separated from the rest. They are excluded from the

**Table 4.** Catalog of NGC 2997 Dwarf Galaxy Candidates

ID	RA (hh:mm:ss)	DEC (dd:mm:ss)	$I$ (mag)	$(V - I)_0$ (mag)	$(B - V)_0$ (mag)	$\mu_{o,I}$ (mag arcsec $^{-2}$ )	$r_{o,I}$ (arcsec)	$n_I$	$r_{e,I}$ (arcsec)	$M_V$ (mag)	Comments <sup>†</sup>
KSP-DW78	9:45:14.2	-30:10:01.2	18.44	0.60	0.45	23.13±0.07	4.92±0.42	0.73±0.14	5.42	-11.39	
KSP-DW79	9:46:12.8	-30:27:51.2	17.98	0.72	0.53	22.39±0.04	5.07±0.27	0.71±0.07	5.36	-11.72	dI
KSP-DW80	9:45:42.8	-30:28:42.9	17.82	0.73	0.69	22.54±0.04	4.43±0.21	0.75±0.06	4.98	-11.88	
KSP-DW81	9:46:15.7	-30:14:29.6	19.25	0.83	0.45	24.12±0.11	6.37±0.62	0.44±0.16	4.91	-10.36	dI
LEDA 718707	9:45:34.9	-30:18:51.3	15.90	0.62	0.50	20.92±0.01	7.05±0.06	0.71±0.01	7.54	-13.91	dI
KSP-DW82	9:44:25.2	-30:12:38.3	18.92	0.58	0.51	23.15±0.05	4.45±0.24	0.56±0.07	3.93	-10.93	
ESO 434-39	9:47:04.2	-30:23:12.5	14.17	0.68	0.53	20.66±0.00	12.22±0.05	0.86±0.01	16.30	-15.58	dI
ESO 434-34	9:45:29.3	-30:20:35.5	13.22	0.60	0.42	21.31±0.00	57.87±0.36	0.55±0.01	50.40	-16.61	dI
KSP-DW83	9:41:05.6	-30:18:45.3	17.23	0.71	0.68	21.61±0.02	3.33±0.11	1.15±0.05	7.32	-12.49	dI
KSP-DW84	9:40:16.3	-30:17:22.7	17.94	0.48	0.45	23.86±0.08	10.31±0.97	0.46±0.17	8.13	-12.0	dI
KSP-DW85	9:40:52.1	-30:00:17.5	19.10	0.87	1.10	23.48±0.08	4.49±0.35	0.49±0.14	3.65	-10.46	
KSP-DW86	9:48:04.3	-31:52:07.1	17.06	0.71	0.29	22.58±0.05	7.13±0.44	0.82±0.09	8.92	-12.66	dI
KSP-DW87	9:47:15.7	-31:47:34.7	19.90	0.83	0.26	23.60±0.09	3.81±0.35	0.54±0.15	3.26	-9.71	
KSP-DW88	9:48:27.9	-31:47:56.3	18.89	0.85	0.68	22.61±0.04	3.12±0.13	0.69±0.06	3.21	-10.69	
KSP-DW89	9:44:38.9	-31:35:28.2	18.30	0.59	0.25	24.47±0.11	11.48±1.12	0.36±0.17	8.21	-11.54	
IC 2507	9:44:34.0	-31:47:22.4	11.82	0.78	0.33	19.55±0.00	23.98±0.13	0.66±0.01	23.71	-17.83	dI
KSP-DW90	9:44:47.2	-31:28:14.5	19.70	0.84	0.65	23.32±0.06	3.67±0.21	0.48±0.09	2.94	-9.89	
KSP-DW91	9:45:28.3	-31:22:47.4	17.88	0.87	0.67	22.25±0.03	2.76±0.19	1.39±0.12	9.65	-11.68	N
KSP-DW92	9:46:21.7	-31:17:03.4	18.56	0.85	0.71	24.10±0.21	9.71±2.90	0.70±0.58	10.19	-11.02	
KSP-DW93	9:46:46.9	-31:05:20.2	20.62	1.08	0.60	24.51±0.16	4.56±0.74	0.52±0.27	3.83	-8.74	
KSP-DW94	9:46:51.8	-31:02:02.0	21.24	1.17	1.57	25.14±0.33	5.69±2.77	0.65±0.89	5.61	-8.02	
KSP-DW95	9:47:51.8	-30:55:44.2	20.00	0.99	0.55	23.44±0.07	2.54±0.25	0.78±0.15	3.00	-9.44	
KSP-DW96	9:47:27.1	-30:56:40.4	16.85	0.89	0.58	21.87±0.03	5.24±0.17	0.64±0.04	5.05	-12.69	
ESO 434-41	9:47:46.4	-31:30:27.6	13.57	0.68	0.34	21.86±0.00	33.60±0.45	0.82±0.02	41.86	-16.18	dI
KSP-DW97	9:40:12.9	-31:50:42.3	17.72	0.58	0.52	22.27±0.03	3.76±0.17	0.78±0.06	4.44	-12.13	
KSP-DW98	9:41:07.5	-31:45:45.1	19.51	0.64	0.65	24.22±0.16	5.60±0.85	0.41±0.22	4.18	-10.29	
KSP-DW99	9:41:32.8	-31:29:04.6	19.98	0.51	0.42	23.27±0.06	3.15±0.23	0.69±0.10	3.26	-9.94	dI
KSP-DW100	9:41:29.6	-31:30:43.3	16.92	0.89	0.75	21.54±0.01	3.80±0.08	0.96±0.03	5.90	-12.63	
KSP-DW101	9:42:56.4	-31:29:46.9	20.83	0.47	0.83	24.71±0.29	3.73±1.20	0.46±0.58	2.93	-9.14	
KSP-DW102	9:39:40.8	-31:08:57.6	20.83	1.06	1.38	23.77±0.10	3.39±0.37	0.59±0.18	3.09	-8.54	
KSP-DW103	9:42:45.7	-30:57:42.3	18.64	0.77	0.51	22.31±0.03	2.63±0.10	0.87±0.05	3.57	-11.03	
KSP-DW104	9:51:17.2	-31:23:59.5	18.91	0.74	0.41	22.48±0.03	2.73±0.13	0.88±0.06	3.72	-10.78	
KSP-DW105	9:51:13.1	-31:07:44.3	17.37	0.82	0.49	21.33±0.01	2.71±0.06	1.10±0.03	5.38	-12.25	dI
KSP-DW106	9:48:24.8	-30:44:47.3	17.68	0.63	0.57	24.59±0.11	25.40±2.60	0.58±0.18	22.86	-12.12	U
KSP-DW107	9:43:44.8	-31:33:43.0	18.56	0.39	0.85	25.36±0.20	16.53±2.58	0.25±0.25	10.65	-11.48	
KSP-DW108	9:44:43.4	-31:26:40.4	16.45	0.69	0.61	21.22±0.01	3.41±0.07	1.19±0.02	8.04	-13.29	dI
KSP-DW109	9:50:50.4	-32:40:48.0	19.07	0.91	0.47	23.68±0.08	5.39±0.47	0.61±0.14	5.03	-10.45	
KSP-DW110	9:48:19.6	-32:40:33.9	17.87	0.82	0.49	23.23±0.04	7.13±0.31	0.52±0.07	5.98	-11.73	
KSP-DW111	9:49:21.7	-32:29:56.1	19.25	0.89	0.62	23.49±0.07	4.75±0.35	0.66±0.11	4.70	-10.29	
KSP-DW112	9:49:29.2	-32:36:38.8	19.10	0.90	0.82	23.34±0.06	4.50±0.29	0.63±0.09	4.32	-10.44	
KSP-DW113	9:50:39.9	-32:37:03.2	19.77	0.93	0.47	23.49±0.06	3.62±0.24	0.53±0.11	3.08	-9.73	
KSP-DW114	9:48:03.9	-32:17:44.1	19.30	0.72	0.42	23.58±0.06	5.05±0.29	0.55±0.09	4.37	-10.41	
KSP-DW115	9:49:07.5	-31:53:39.3	19.90	0.61	0.37	23.52±0.07	3.22±0.27	0.61±0.12	3.01	-9.92	
KSP-DW116	9:49:49.3	-32:26:55.5	15.86	0.96	0.64	21.78±0.02	8.04±0.18	0.86±0.03	10.75	-13.61	
KSP-DW117	9:45:34.7	-32:21:37.1	19.03	0.85	0.58	23.48±0.06	4.85±0.33	0.53±0.09	4.10	-10.55	
KSP-DW118	9:47:33.0	-32:24:00.6	20.28	0.89	0.71	23.42±0.09	2.61±0.27	0.59±0.15	2.39	-9.25	
KSP-DW119	9:45:40.3	-32:00:30.7	17.90	0.92	0.45	22.93±0.03	8.80±0.28	0.45±0.05	6.87	-11.61	dI
KSP-DW120	9:44:06.2	-31:59:11.5	19.54	0.80	0.82	22.97±0.04	2.59±0.15	0.75±0.07	2.91	-10.09	
KSP-DW121	9:43:31.9	-32:00:59.2	19.80	0.88	0.79	24.01±0.12	4.67±0.63	0.67±0.19	4.69	-9.75	
KSP-DW122	9:45:46.7	-32:10:44.0	19.18	0.73	0.64	22.79±0.04	3.68±0.21	0.81±0.08	4.49	-10.53	dI
KSP-DW123	9:47:13.9	-32:02:07.7	16.26	0.84	0.61	21.98±0.02	7.84±0.17	0.72±0.03	8.47	-13.33	
KSP-DW124	9:46:44.0	-32:35:41.6	17.24	0.82	0.66	22.52±0.03	7.18±0.31	0.86±0.06	9.55	-12.38	
ESO 434-33	9:44:47.6	-31:49:32.0	12.08	0.66	0.35	21.52±0.01	49.43±0.54	0.41±0.01	36.99	-17.69	dI
ESO 434-27	9:44:05.2	-32:09:54.3	13.86	0.75	0.55	22.06±0.01	25.50±0.43	0.86±0.02	33.76	-15.83	dI
KSP-DW125	9:42:51.9	-31:58:46.2	19.82	0.73	0.81	23.17±0.06	2.65±0.22	0.79±0.12	3.19	-9.88	

<sup>†</sup> Candidates identified as UDG (U), Nucleated (N), or irregularly shaped (dI).

$I$  and  $M_V$  are apparent  $I$ -band magnitude and absolute  $V$ -band magnitude, respectively, estimated using the fitted parameters of the Sérsic function.  $\mu_{o,I}$ ,  $r_{o,I}$ , and  $n_I$  are the central surface brightness, scale length, and the Sérsic index from the fitting of  $I$ -band images, respectively.  $r_{e,I}$  is the effective radius obtained from  $r_{o,I}$  and  $n_I$ .  $(V - I)_0$  and  $(B - V)_0$  are the observed mean colors after correction of the reddening in the Milky Way.

3-sigma clipping process during the calculation of mean colors to minimize the effects of potential outliers.

## 4.2 Color and Structure Parameters

Figure 7 presents the color-magnitude diagrams, i.e.,  $(B - V)_0$  vs.  $M_V$  (top panel) and  $(V - I)_0$  vs.  $M_V$  (bottom panel), for all the DGCs from the four groups: NGC 2784 (open squares; Park et al. 2017), NGC 3585 (open triangles; Park et al. 2019), NGC 2997 (filled red circles), and M83 (open diamonds; Müller et al. 2015). The mean

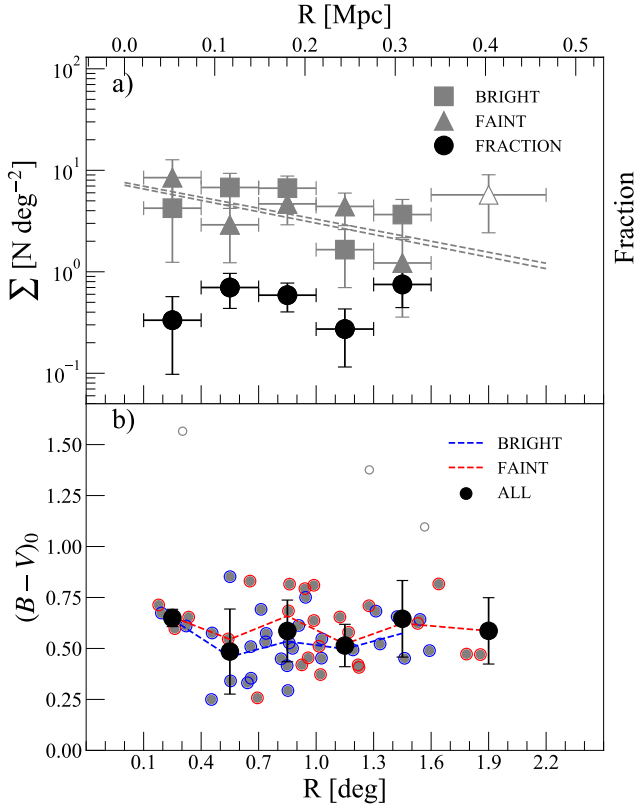


**Figure 6.** *Upper Panel:* Radial number density distributions of bright (squares) and faint (triangles) groups of the DGCs in the NGC 2997 group divided by  $M_V = -11.02$  mag. The circles show the distribution of the bright-to-faint ratio. *Lower Panel:* Radial color distribution of the DGCs. The small circles show the radial distances and the  $(B - V)_0$  colors of the entire 55 DGCs population. Those encased by red and blue circles are the faint and bright members, respectively. (Three out of fifty-five are open circles, while the rest are filled). The black solid circle, red and blue dashed lines are the mean color distributions of the entire sample, faint sample, and bright sample, respectively. The three small unfilled circles are excluded in the mean color calculations in order to avoid potential contributions from outliers.

values of the  $(B - V)_0$  and  $(V - I)_0$  colors are respectively  $0.66 \pm 0.16$  and  $0.84 \pm 0.18$  mag for NGC 2784,  $0.69 \pm 0.18$  and  $0.87 \pm 0.14$  mag for NGC 3585, and  $0.56 \pm 0.15$  and  $0.77 \pm 0.16$  mag for NGC 2997, while the  $(B - V)_0$  color of M83 is  $0.82 \pm 0.25$  mag. The dashed blue lines in Figure 7 represent the color-magnitude relation (CMR) for the DGCs brighter than  $M_V = -11$  mag in the NGC 2784 and NGC 3585 groups (Park et al. 2019), with slopes of  $-0.012$  and  $-0.013$  for  $(B - V)_0$  and  $(V - I)_0$  colors, respectively. These slopes change to  $\approx 0$  when we also include the DGCs from the NGC 2997 group (solid red lines), indicating that the DGCs in the NGC 2997 group have opposite CMRs to those of NGC 2784 and NGC 3585.

We examine the correlation between the two parameters (i.e., color vs. absolute magnitude) of the CMR of each group as follows. For the  $(B - V)_0$  color (Figure 8), the best-fit CMR slopes and the linear correlation coefficients are  $-0.01 \pm 0.02$  and  $-0.12$  (NGC 2784),  $-0.01 \pm 0.02$  and  $-0.06$  (NGC 3585),  $0.03 \pm 0.01$  and  $0.41$  (NGC 2997),  $0.04 \pm 0.02$  and  $0.33$  (M83). These results show a clear distinction that the brighter DGCs appear bluer in the two groups with a late-type spiral host (i.e., NGC 2997 and M83), while they show an opposite pattern in the other two groups with an early-type elliptical host (i.e., NGC 2784 and NGC 3585). The correlation between the color and

magnitude is much stronger in NGC 2997 and M83. For the  $(V - I)_0$  color (Figure 9), the best-fit CMR slopes and the linear correlation coefficients are  $0.003 \pm 0.02$  and  $0.03$  (NGC 2784),  $-0.007 \pm 0.01$  and  $-0.08$  (NGC 3585),  $0.004 \pm 0.01$  and  $0.05$  (NGC 2997). We find that correlations in general are much weaker for the  $(V - I)_0$  colors, and the slopes are essentially flat.

Recent large surveys have estimated structural properties of satellites for a large number of MW-like systems (e.g. SAGA and ELVES, Mao et al. 2021; Carlsten et al. 2021b, 2022). In Figure 10, we show the distributions of structural parameters—the central surface brightness  $\mu_{o,V}$  (top panel), the effective radius  $r_e$  (middle panel), and the Sérsic curvature index  $n$  (bottom panel)—for DGCs of NGC 2784, NGC 3585, NGC 2997 from our studies, M83 from Müller et al. (2015), together with those of the 444 satellites around MW-like systems from the ELVES survey (Carlsten et al. 2022) as a function of their  $V$ -band absolute magnitudes. (Note that individual data values of the Sérsic curvature indices for the ELVES satellites are unavailable other than a median value of 0.72 (Carlsten et al. 2021b); thus, they are not included in the bottom panel.) As expected, we can first identify that most of the DGCs in the collected sample reside within the completeness boundary curves (gray dashed curves in Figure 10) for  $\mu_{o,V}$  and  $r_e$  calculated using the following equations from Ferguson & Sandage (1988); Müller et al. (2015):

$$M_V = \mu_{o,V} - 5 \log(r_{\text{lim}}) - 2.18 + 5 \log(\mu_{\text{lim}} - \mu_{o,V}) \quad (1)$$

$$M_V = \mu_{\text{lim}} - \frac{r_{\text{lim}}}{0.5487 r_{e,V}} - 2.5 \log[2\pi \times (0.5958 r_{e,V})^2] \quad (2)$$

where  $\mu_{\text{lim}}$  and  $r_{\text{lim}}$  are the limiting surface brightness and the limiting radius size for our images and detection. The equations are based on the assumption that galaxies are well-fit by an exponential Sérsic profile, which is the case for the 55 DGCs in our study. We use  $r_{\text{lim}} \approx 4''$  for the limiting size, which is based on our visual selection criteria (see § 3.1). We obtain  $\mu_{\text{lim},V} = 28$  mag arcsec $^{-2}$  for the limiting surface brightness using the following relation from Román et al. (2020) at 3- $\sigma$  level:

$$\mu_{\text{lim}} = -2.5 \times \log(3\sigma / \text{pix} \times \Omega) + \text{zero} \quad (3)$$

where  $\sigma$ ,  $\text{pix}$ , and  $\Omega$  represent the standard deviation of the sky level, the pixel size of our images ( $= 0.4$  arcsec, see § 2), and an angular scale of 8.0 arcsec ( $2 \times r_{\text{lim}}$ , see § 3.1) while  $\text{zero}$  is the zero point offsets of our images (see Table 2). This confirms that the distributions of structure parameters of NGC 2997 DGCs from our study conform to the predictions on detection limits by Ferguson & Sandage (1988). The one DGC located outside the boundary curve is DW94 from NGC 2997, and it is very faint (See Figure A1). Both the two structure parameters, i.e.,  $\mu_{o,V}$  and  $r_e$ , of DGCs from our studies and satellites from ELVES survey in Figure 10 appear to increase as the  $V$ -band luminosity increases. The median value of the Sérsic curvature index of the DGCs from NGC 2997 is 0.68, largely consistent with 0.8 for NGC 2784 and NGC 3585, as well as 0.72 for the satellites from the ELVES survey (Carlsten et al. 2021b). It is a bit smaller than 1.1 for M83, but still not significantly different. This similarity and consistency of the structure parameters from our studies and the ELVES survey for the dwarf galaxies of MW-like systems is encouraging and may indicate the presence of common patterns in their properties. Future investigation of their distributions and properties using more statistically significant samples can lead to advanced understanding of their origin and evolution and provide important information for our understanding of challenges that the current  $\Lambda$ CDM model faces (e.g., Weinberg et al. 2015).

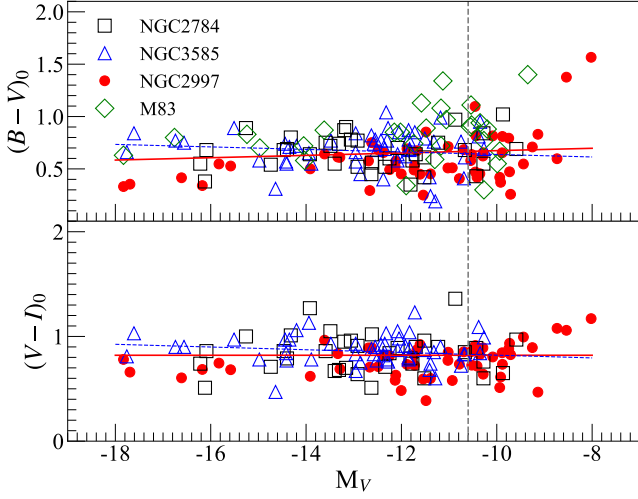


**Figure 7.** Color-magnitude diagrams. Color-magnitude diagram of the DGCs in NGC 2997 (red filled circles) compared with those of the NGC 2784 (squares, Park et al. 2017), NGC 3585 (triangles, Park et al. 2019), and M83 (diamonds, Müller et al. 2015). The blue dashed line represents the best-fit linear relation obtained in Park et al. (2019) using the DGCs from both NGC 2784 and NGC 3585 groups. The red solid line represents the best-fit linear relation that we obtain from the DGCs of NGC 2997, NGC 2784, and NGC 3585 together. The vertical dashed lines indicate the 90% completeness boundaries (see § 3.1).

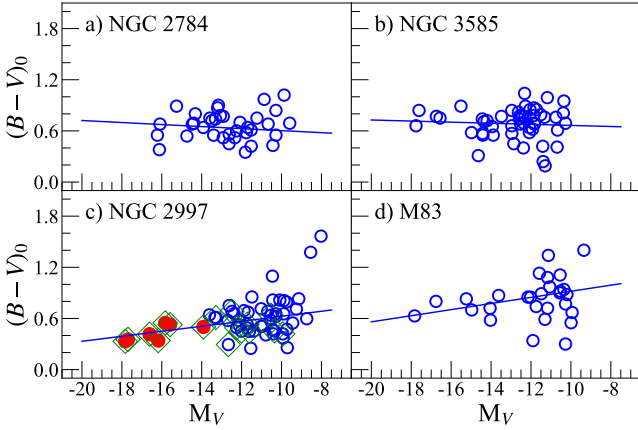


**Figure 8.**  $(B - V)_0$  vs.  $M_V$  color-magnitude diagrams of the DGCs in NGC 2784 (Park et al. 2017), NGC 3585 (Park et al. 2019), NGC 2997 (this work), and M83 (Müller et al. 2015) shown in circles. The blue solid lines represent the best-fit linear relation with  $3\text{-}\sigma$  clipping that we obtain between the two parameters. In panel c), the red circles mark the 7 previously discovered dwarf galaxies (Table 3). The circles with a green diamond are those morphologically identified as irregular, while the rest are elliptical.

### 4.3 Luminosity Function

In Figure 11 (top panel), we show a cumulative LF of the NGC 2997 group constructed with 52 DGCs that we used for the radial number density distribution analysis (Figure 5), excluding three DGCs in the last radial bin, together with  $M_V \approx -20.65$  mag for NGC 2997 itself (de Vaucouleurs & Longo 1988). The 52 DGCs are at projected distances  $\leq 400$  kpc, which is the virial radius of the group, and include all of the previously-discovered members. The dashed line in

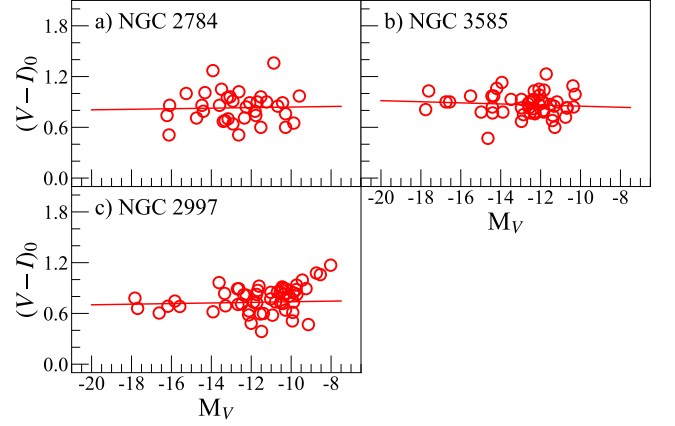


**Figure 9.** Same as Figure 8, but for  $(V - I)_0$  vs.  $M_V$  for NGC 2784, NGC 3585, and NGC 2997. The red solid lines are the best-fit linear relations that we obtain between the parameters.

the top panel of Figure 11 represents the best-fit Schechter function with a faint-end slope of  $\alpha = -1.43 \pm 0.02$  obtained by fitting the LF where  $M_V \leq -10$  mag, as was done in our previous studies, using the non-linear least-square fitting method. The shaded region shows the area for  $M_V \gtrsim -10.6$  mag, which is the 90% completeness magnitude limit of our detection (§ 3.1). The slope of the LF for the faint dwarf galaxy candidates in this area becomes more flattened as the luminosity decreases, indicating that the flattening is at least partially attributed by the incompleteness of our detection for  $M_V \gtrsim -10.6$  mag.

We explore the effects of background contamination, which become more substantial for the population of faint dwarf galaxies, to our measurement of the faint-end LF slope above. According to the recent results from the ELVES survey, low luminosity ( $M_V$ ) dwarf galaxies with higher central surface brightness ( $\mu_{0,V}$ ) are more likely to be contaminants than those with lower central surface brightness (Carlsten et al. 2022). As described in § 3.1, we expect 7–16 background contaminants out of the 55 DGCs that we identified in the NGC 2997 field. If we assume that there are 16 contaminants in our sample of 55 DGCs and that all of them follow the same pattern of stellar-mass dependent contamination-likelihood found by the ELVES survey, we estimate the contamination-corrected LF slope of the NGC 2997 group to be  $-1.23 \pm 0.03$ . For this, we identify 16 DGCs in our sample that are more likely contaminants than others and exclude them in the LF slope fitting as follows: we first establish a linear relation between  $M_V$  and  $\mu_{0,V}$  among the 55 DGCs, and then select 16 DGCs that have largest excess in  $\mu_{0,V}$  to the linear relation. We only select DGCs that are fainter than  $M_V = -12.5$  mag, which is the expected upper magnitude limit for our background contaminants (see § 3.1). The final 16 DGCs chosen as contaminants have excess  $\mu_{0,V}$  by more than  $0.25$  mag arcsec $^{-2}$  when compared to the expected values from the linear relation. The background contamination-corrected faint-end slope is about 0.2 shallower than the slope measured without such correction. Since 16 is the upper limit for the number of background contaminants, we expect the true value of the faint-end LF slope after stellar-mass dependent correction to be between  $-1.43$  and  $-1.23$ .

The bottom panel of Figure 11 compares the cumulative LF of NGC 2997 with those of NGC 2784 (Park et al. 2017), NGC 3585 (Park et al. 2019), and M83 (Müller et al. 2015). Applying the same fitting method, we obtain their best-fit LF faint-end slopes to be –

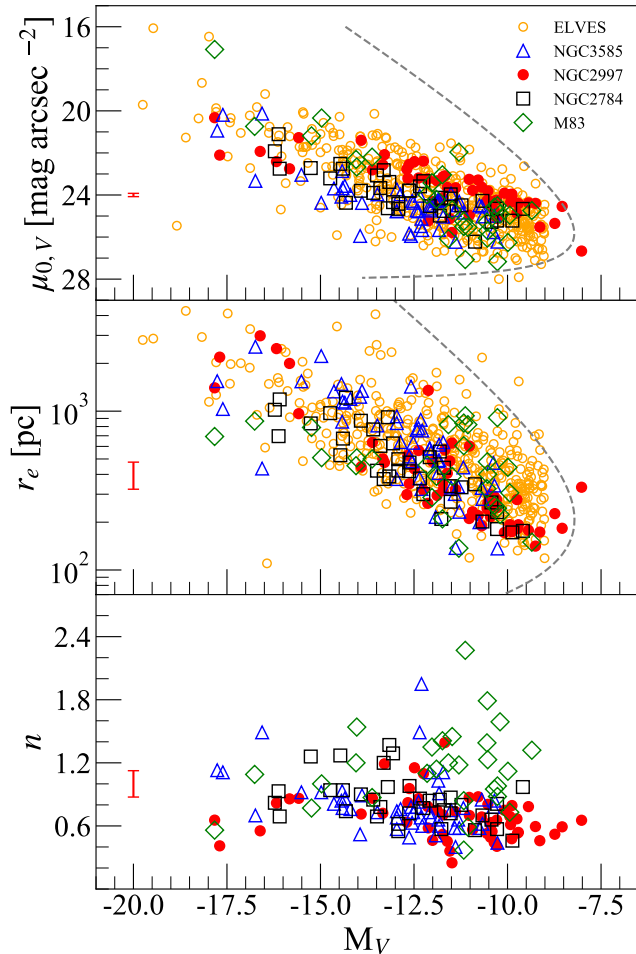


**Figure 10.** Distributions of the apparent central surface brightness ( $\mu_{0,V}$ ; top panel), effective radii ( $r_e$ ; middle panel), and Sérsic indices ( $n$ ; bottom panel) along the  $V$ -band absolute magnitudes ( $M_V$ ) of the DGCs in NGC 2784 (squares), NGC 3585 (triangles), NGC 2997 (filled circles), M83 (diamonds). The gray dashed lines in the top and middle panels are the completeness boundaries. The red error bars in the left-hand part of each diagram represents the mean uncertainties of the parameters for the candidates in NGC 2997.

$1.22 \pm 0.03$  (NGC 2784),  $-1.33 \pm 0.03$  (NGC 3585), and  $-1.40 \pm 0.04$  (M83). The faint-end slope of NGC 2997 is very similar to that of M83, while it is a bit steeper than those of NGC 2784 and NGC 3585. Compared to the range of  $-1.9 \lesssim \alpha \lesssim -1.6$  typically predicted by  $\Lambda$ CDM models (e.g., Klypin et al. 1999; Trentham & Tully 2002; Springel et al. 2008; Han et al. 2016; Li et al. 2019), the faint-end LF slopes of these galaxies appear to be consistently flatter. However, we note that recent  $\Lambda$ CDM simulations based on different types of stellar-to-halo mass relation, which is still poorly constrained for low-mass dwarf galaxies, have shown that there exists a great uncertainty in the predicted LFs (e.g., Carlsten et al. 2021a). It is, therefore, premature to ascertain whether the slope that we measure for the NGC 2997 group is in an agreement or disagreement with  $\Lambda$ CDM model prediction.

Figure 12 shows the distributions of the LFs for bright ( $M_V \lesssim -12.1$  mag) satellites around 11 MW-like galaxies: four (NGC 6181, 6278, 5297, and 7166; shown in blue-hued circles and lines) from the SAGA survey, four (NGC 3627, 3379, 1808, and 1291; purple-hued circles and lines) from the ELVES survey, and three (NGC 2784,

3585, and 2997; red-hued symbols and dashed lines) from the KSP (including this study). The SAGA groups consist of the 4 most populated groups from the survey in terms of the number of confirmed satellites, while the 4 groups from the ELVES survey are selected because they have distances similar to that of NGC 2997 with a satellite survey size comparable to that of the SAGA survey, i.e.,  $R \lesssim 300$  kpc. We can identify in the figure that the LFs of the three KSP group members, which are similar to each other, lie between those of the ELVES groups for faint regime of  $M_V \gtrsim -14$  mag with more rapid increase in number of satellites as they become fainter. The LF slopes of the KSP and the two ELVES groups appear to be much steeper than that of the SAGA survey in this faint regime. According to (Carlsten et al. 2022), this might have been caused by incompleteness beyond what is accounted for in the SAGA survey, especially in the low-mass regime (see the reference for the details). As we explained in § 3.1, the detection rate of bright satellites from our work on NGC 2997 is similar to that of the SAGA survey, which we can confirm in their LFs in Figure 12. Two galaxy groups, which are NGC 3379 and NGC 3627, from the ELVES survey have brightest ( $< -20$  mag) satellites as well as the largest number of faint ones, confirming that groups with brighter satellites tend to have a larger number of satellites, as have been found in recent studies (Mao et al. 2021; Carlsten et al. 2022).

There exists no DGC in our sample that has  $M_V$  around  $-15$  mag (Table 4), which we identify as a 2-mag gap-like feature near  $M_V = -15$  mag in the LF. In the SAGA survey of small galaxy groups (Geha et al. 2017), the majority of the groups show similar magnitude gaps in the range of 2.2–3.6 mag, consistent with the prediction by numerical simulations presented in the same work, while a small number of faint (i.e.,  $M_K \gtrsim -23.75$  mag for the host galaxy luminosity) groups have gaps greater than 5 mag. Considering that NGC 2997 is MW-analogous with  $M_K \simeq -24.02$  mag (§1) similar to the systems studied in the SAGA survey, the 2.2 mag gap-like feature in the LF of NGC 2997 may indicate the presence of a similar gap among small MW-analog groups (see also Bennet et al. 2019). In order to examine the statistical significance of the gap-like feature in NGC 2997, we perform a p-value test on 100,000 cases of randomly-sampled 55 dwarf galaxies from a Schechter function constructed by using the LF parameters of NGC 2997 group. As a result, we find that about 60 % of the 100,000 cases have the presence of such a gap in their LFs, meaning the gap-like feature in the LF of NGC 2997 is more likely a result of random sampling with small statistical significance.

## 5 EVOLUTIONARY STAGE OF THE NGC 2997 GROUP

The DGCs that we identify in the field of NGC 2997 show several notable characteristics diagnostic of their evolutionary stage as we discuss below.

### 5.1 Color-Magnitude Relation, Star Formation Activities, and Galactic Conformity

The CMR of the DGCs in NGC 2997 indicates that the group is populationally young with ongoing star formation activities. Their  $(B - V)_0$  colors show a positive correlation with  $M_V$  (Figure 8; §4.2) with brighter members being bluer, and this suggests the presence of younger stellar populations in the brighter and more massive members, indicating that the star-formation activities in less massive members are more quenched than their massive counterparts. Since most of our candidates are within the virial radius ( $\simeq 400$  kpc) of

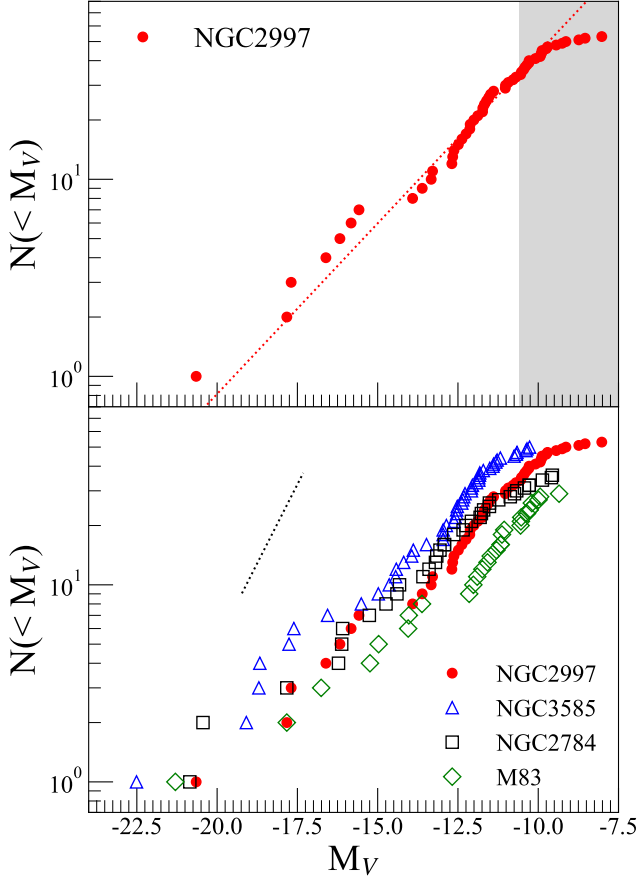


**Figure 11.** (Top) The cumulative LF (red filled circles) of the NGC 2997 group. The dotted line represents the best-fit Schechter function with the faint-end slope  $\alpha \approx -1.43$ . The shaded area indicates the magnitude region below our work’s 90% completeness magnitude limit ( $M_V \gtrsim -10.6$  mag). (Bottom) The cumulative LFs of NGC 2997 compared with those of NGC 2784 (squares; Park et al. 2017), NGC 3585 (triangles; Park et al. 2019), and M83 (diamonds; Müller et al. 2015). The black dotted line is the case of  $\alpha = -1.8$  predicted by the  $\Lambda$ CDM model (Trentham & Tully 2002).

NGC 2997, it is likely that their quenching is caused by the group environmental effects. This interpretation is further supported by various observational results showing a clear contrast in quenching between field and satellite dwarf galaxies: the former have shown an extreme lack of quenching (e.g. Weisz et al. 2011; Geha et al. 2012), whereas the latter have shown much stronger environmental quenching (e.g., see Fillingham et al. 2018, and references therein). Given that the timescale of environmental quenching is much shorter for lower mass satellites (e.g., Samuel et al. 2022), it is conceivable that only the low-mass members of the group have had enough time for the environmental quenching to develop, causing them to appear redder than the massive members.

It is known that colors of shorter wavebands (e.g.,  $B - V$ ) are more affected by star formation activities (or stellar age variations) than those in longer wavebands (e.g.,  $V - I$ , see Chang et al. 2006; Janz & Lisker 2009, for example). The  $(V - I)_0$  colors of DGCs in the NGC 2997 group show a much weaker correlation with their luminosity than  $(B - V)_0$  color does (§4.2), supporting the interpretation that the CMR of NGC 2997 could be primarily driven by star formation activities, and hence stellar age variations. Similar relations between the color and magnitudes of satellite galaxies to

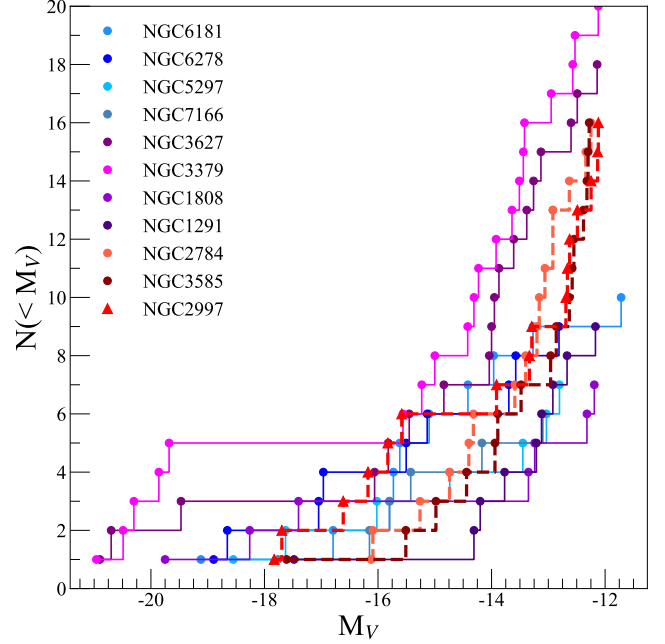


**Figure 12.** Luminosity function of NGC 2997 compared with those of sample galaxies from the SAGA and ELVES surveys as well as from our previous studies (see § 4.3). The purple-hued points and lines are the groups from the ELVES survey, while the blue-hued points and lines are the groups from the SAGA survey. The red points and dashed lines are the groups from the KSP survey.

those of NGC 2997 have been found in many recent observational and simulation studies. More massive satellites found in the ELVES survey around MW-like hosts appear systematically bluer than the less massive members (Carlsten et al. 2022), consistent with the measurements made by  $H\alpha$  showing that the quenched fraction decreases as the mass of satellites increases. Recent FIRE-II simulation of cosmological galaxy formation (e.g. Samuel et al. 2022) has also found that massive satellites around MW-like galaxies have significantly lower quenched fractions compared to less massive members. The results from these observational and simulation studies are in line with our interpretation that the more massive DGCs of NGC2997 have experienced less quenching. Additionally, there also exists a higher fraction of irregular morphologies among the brighter DGCs in NGC 2997 (§3.3 and §5.3), further supporting this interpretation since irregular galaxies in general appear to have more persistent star formation activities (Chiboucas et al. 2009; Kormendy & Bender 2012; Kirby et al. 2013; Lassen et al. 2021; Carlsten et al. 2021c). These observed properties of the DGCs in NGC 2997 suggest that the brighter dwarf galaxies in NGC 2997 are more dominated by star-forming late-type galaxies with younger stellar age.

The average  $(g - r)_0$  color of the 127 satellite galaxies identified in the SAGA survey around 36 MW-analog hosts with the detection limit of  $M_r \lesssim -12.3$  mag is  $0.39 \pm 0.13$  mag (Mao et al. 2021), which converts to  $B - V \approx 0.61 \pm 0.13$  mag when adopting the conversion relation between  $g - r$  and  $B - V$  colors (Jester et al. 2005). (Note that, according to (Jester et al. 2005), the rms conversion uncertainty between these two colors is small at the level of 0.04 mag.) In our study, the average  $(B - V)_0$  color of the 18 brightest DGCs of NGC 2997 with  $M_V \lesssim -12$  mag, which is equivalent to the SAGA detection limit above, is  $0.52 \pm 0.13$  mag. The bright

DGCs in NGC 2997 have comparable  $(B - V)_0$  colors to those of the SAGA satellites. Considering that most of the SAGA satellites have apparent star formation activities, this could also indicate that the bright DGCs in NGC 2997 have active star formation activities, consistent with our interpretation that they are mostly star-forming late-type galaxies.

The CMR pattern of NGC 2997 from our study appears to be different from those of NGC 2784 and NGC 3585 from our previous studies in that the  $(B - V)_0$  colors and luminosity of the DGCs of the two early-type hosted groups show weak, negative correlations (Park et al. 2017; Park et al. 2019). We note, however, that the DGCs of the M83 group, which has a late-type host like NGC 2997, show a strong, positive correlation between  $(B - V)_0$  and luminosity, similar to NGC 2997 (Figure 8), indicating more active star-formation activities in more massive members. It appears, therefore, that the DGCs in the groups of NGC 2784, NGC 3585, and NGC 2997 as well as M83 show star-formation activities that are overall similar to those of their hosts, compatible with “galactic conformity” wherein satellite galaxies tend to show similar star-formation activities and colors to their hosts (Weinmann et al. 2006; Bray et al. 2016; Treyer et al. 2018).

## 5.2 Radial Distribution of Mass and Color

As seen in Figure 6, there appears to be no apparent segregation in mass and color of the DGCs in NGC 2997, showing that the DGCs near the center of the group are neither particularly more massive nor redder. In some cluster and groups, the central area near the host is predominantly populated by more massive satellites (Presotto et al. 2012; Roberts et al. 2015; Joshi et al. 2016; Barsanti et al. 2018; Kim et al. 2020), often attributed to the stronger effects of dynamical friction (Chandrasekhar 1943). However, some previous studies have also found no signs of mass segregation in other clusters and groups (von der Linden et al. 2010; Vulcani et al. 2013; Kafle et al. 2016). It has been suggested that gas-stripping environmental effects, i.e. ram pressure and tidal stripping (Kafle et al. 2016; Barsanti et al. 2018; Kim et al. 2020), could lead to less efficient dynamical friction and mass segregation. In the case of NGC 2997 group, which is located in a low-density environment of the loose group LGG 180 (see § 1) without any detected diffuse X-ray emission (Sengupta & Balasubramanyam 2006), the gas stripping processes are likely relatively inefficient, which is compatible with the known insignificant deficiency of  $H_I$  gas in LGG 180 galaxies (Sengupta & Balasubramanyam 2006; Pisano et al. 2012; Pisano 2014), making dynamical friction more prevalent. We estimate the dynamical friction time-scale for brighter ( $M_V \lesssim -15$  mag) and fainter members of the NGC 2997 group to be about 7 Gyrs in average and longer than the Hubble time, respectively, assuming a uniform light-to-mass ratio and following the method in Jiang et al. (2008). One feasible scenario explaining the absence of mass segregation in the NGC 2997 group is that its massive members have been accreted onto the group halo recently during the last 7 Gyrs. Similar to our scenario, some studies (see Barsanti et al. 2018, for example) of small group environments (like NGC 2997, § 1) have strongly suggested that massive star-forming satellites are likely new members recently accreted from surrounding fields. Since recently accreted field dwarf galaxies have higher star-formation activities and bluer colors (e.g. Weisz et al. 2011; Geha et al. 2012; Barsanti et al. 2018), this interpretation is also consistent with our CMR (see § 5.1).

The  $(B - V)_0$  color distribution of the DGCs in NGC 2997 along the radial distance from the host is overall flat (Figure 6, bottom panel) without any apparent radial dependency, which is in contrast to what

can be expected for an evolved system where earlier and stronger quenching of star formation driven by stronger tidal forces and also by more effective interactions with the intracluster medium (Wetzel et al. 2013; Park et al. 2017) would cause satellite galaxies near the center to be redder than those at larger distances (e.g., Presotto et al. 2012; Lisker et al. 2013; Lee et al. 2016). For example, according to the study by De Lucia et al. (2012) based on the Millennium Simulation, a much steeper radial color distribution is plausible for dwarf galaxies that have been satellites for over at least 5–8 Gyrs. The absence of color segregation among the NGC 2997 DGCs, therefore, could be consistent with the scenario that some of them are newly accreted members. This is also inline with our interpretation above for the absence of mass segregation in which we suggest that the massive members of NGC 2997, which are blue (Figure 8), are recently accreted. Another possible explanation for the origin of the observed shallow color gradient of NGC 2997 is less efficient quenching for a late-type system (Weinmann et al. 2006; Bray et al. 2016; Treyer et al. 2018) in that a shallow color gradient may simply results from similar star formation activities between the host and satellites, known as “galactic conformity.” However, it is not clear how this process can explain the observed absence of mass segregation in NGC 2997. Overall, the absence of mass and color segregation in NGC 2997 appears to be compatible with the scenario that the system has recently accreted massive, blue dwarf galaxies, possibly from the surrounding field.

## 5.3 Morphologies

Another notable characteristic of the DGCs of NGC 2997 group is their morphology. While we identify only one UDG and one nucleated dwarf galaxies (see § 3.3) in the NGC 2997 group, ten and four of the DGCs in NGC 3585 are nucleated and UDGs, respectively (Park et al. 2019). In addition, as shown in § 3.1 and Figure 8, NGC 2997 appears to have a higher ratio of morphologically irregular dwarf galaxies (dIs) — the fraction of dIs is  $31\% \pm 9\%$  in NGC 2997, while it is  $18\% \pm 8\%$  and  $11\% \pm 7\%$  in NGC 2784 and NGC 3585 when adopting the same selection criteria (See § 3.3), respectively. These potential differences in the morphology of the DGCs between the NGC 2997 system and the other two appear to be consistent with our interpretation that this system is in a low-density environment, and it is populationally young with recent accretion of new dwarf galaxies. First, the relative paucity of the nucleated dwarf galaxies can be understood in populationally young satellite galaxies where there has not been enough time for globular clusters to infall to form nucleus (Oh & Lin 2000; Fahrion et al. 2021; Poulain et al. 2021). Secondly, it might be difficult to develop UDGs in a low density environment (LGG 180) via tidal stripping of gas and/or their size expansion through tidal heating (Tremmel et al. 2020; Jones et al. 2021). Thirdly, the higher fraction of dIrrs among the DGCs in NGC 2997 is compatible with a them being newly accreted dwarf galaxies where there has not been enough time for them to evolve into more early-type morphologies (Pasetto et al. 2003; Dunn 2010; Chattopadhyay et al. 2015; Carlsten et al. 2021c).

## 6 SUMMARY AND CONCLUSION

In the work presented in this paper, we conduct photometric analysis of 55 DGCs that we have identified in the field of the giant spiral galaxy NGC 2997 using the deep stacked images obtained from the KMTNet Supernova Program. Out of 55, 48 are newly discovered in this work while the rest seven are already identified candidates from

previous studies. Table A1 compares the parameters of the DGCs in the NGC 2997 group that we identify in this study to those of the NGC 2784 and NGC 3585 groups. We summarize our main results below, along with our conclusions about the evolutionary stage of the NGC 2997 group based on our results.

- The 55 candidates show a broad range of photometric and structural parameters that are overall compatible with those found from the dwarf galaxies in other galaxy groups. Their  $I$ -band effective radii,  $I$ -band Sérsic index, and the  $V$ -band total absolute magnitudes range from 0.142 to 2.97 kpc, from 0.25 to 1.39, and from  $-8.02$  to  $-17.69$  mag, respectively. The faint-end slope of their luminosity function is  $\alpha = -1.43 \pm 0.02$ , which is shallower than predictions based on  $\Lambda$ CDM models, but largely comparable with previously measured values. (§ 3.2, § 4.3)

- The DGCs of the NGC 2997 group are bluer than those of the NGC 2784 and NGC 3585, with its brighter members being systematically bluer than the fainter ones. The inferred higher star-formation activities in the more massive members of the NGC 2997 group could result from them having experienced group environmental quenching for a shorter time. (§ 5.1)

- The projected number density of the DGCs in NGC 2997 group decreases along the distance from the center of NGC 2997, and there is no difference in this radial number density distribution between the bright ( $M_V \lesssim -11.02$  mag) and faint members of the group. The average color of them appears to be invariant as a function of the radial distance. The lack of mass or color segregation again appears to be compatible with the scenario that the system has recently accreted massive, blue dwarf galaxies, possibly from the surrounding field. (§ 5.2)

- Compared to our previous studies of DGCs in the field of NGC 2784 and NGC 3585 using similar KMTNet data, the DGCs of NGC 2997 show a lack of more morphologically developed candidates — out of the 55 candidates, we are able to identify only one ultra-diffuse dwarf galaxy, and one nucleated candidates. In contrast, there exists a significantly increased fraction of irregularly shaped candidates (17 in total) in our sample of NGC 2997, and they are significantly more luminous and bluer. These morphological distributions of the DGCs indicate that the NGC 2997 group is populationally young with recently accreted luminous dwarf galaxies. (§ 5.3)

- For the brighter DGCs in NGC 2997, we find their detection rate and the inferred star formation activities are largely comparable to those found in the SAGA survey, whose detection limit is  $M_V = -12.1$  mag, of MW-analog groups in the distance range 25–42 Mpc. Similar to the results from the SAGA and also to the ELVES survey, the faint DGCs in NGC 2997 appear to be substantially more quenched than bright ones. Identification of whether this trend of quenched star formation activities among faint DGCs in NGC 2997 is a general property of faint satellites around MW-analog hosts requires more samples.

## ACKNOWLEDGMENTS

We are very grateful to the anonymous referee for the thorough and valuable comments that helped improve this paper significantly. This research has made use of the KMTNet system operated by the Korea Astronomy and Space Science Institute (KASI) at three host sites of CTIO in Chile, SAAO in South Africa, and SSO in Australia. Data transfer from the host site to KASI was supported by the Korea Research Environment Open NETWORK (KREONET). We acknowledge with thanks the variable star observations from the AAVSO International Database contributed by observers worldwide and used in

this research. DSM was supported in part by a Leading Edge Fund from the Canadian Foundation for Innovation (project No. 30951) and a Discovery Grant (RGPIN-2019-06524) from the Natural Sciences and Engineering Research Council (NSERC) of Canada. HSP was supported in part by the National Research Foundation of Korea (NRF) grant funded by the Korea government (MSIT, Ministry of Science and ICT; No. NRF-2019R1F1A1058228). Y.D.L. acknowledges support from Basic Science Research Program through the National Research Foundation of Korea (NRF) funded by the Ministry of Education (2022R111A1A01054555). This research was supported by the Korea Astronomy and Space Science Institute under the R&D program (Project No. 2023-1-868-03) supervised by the Ministry of Science and ICT.

## DATA AVAILABILITY

The data underlying this article will be publicly available online once it is accepted for publication.

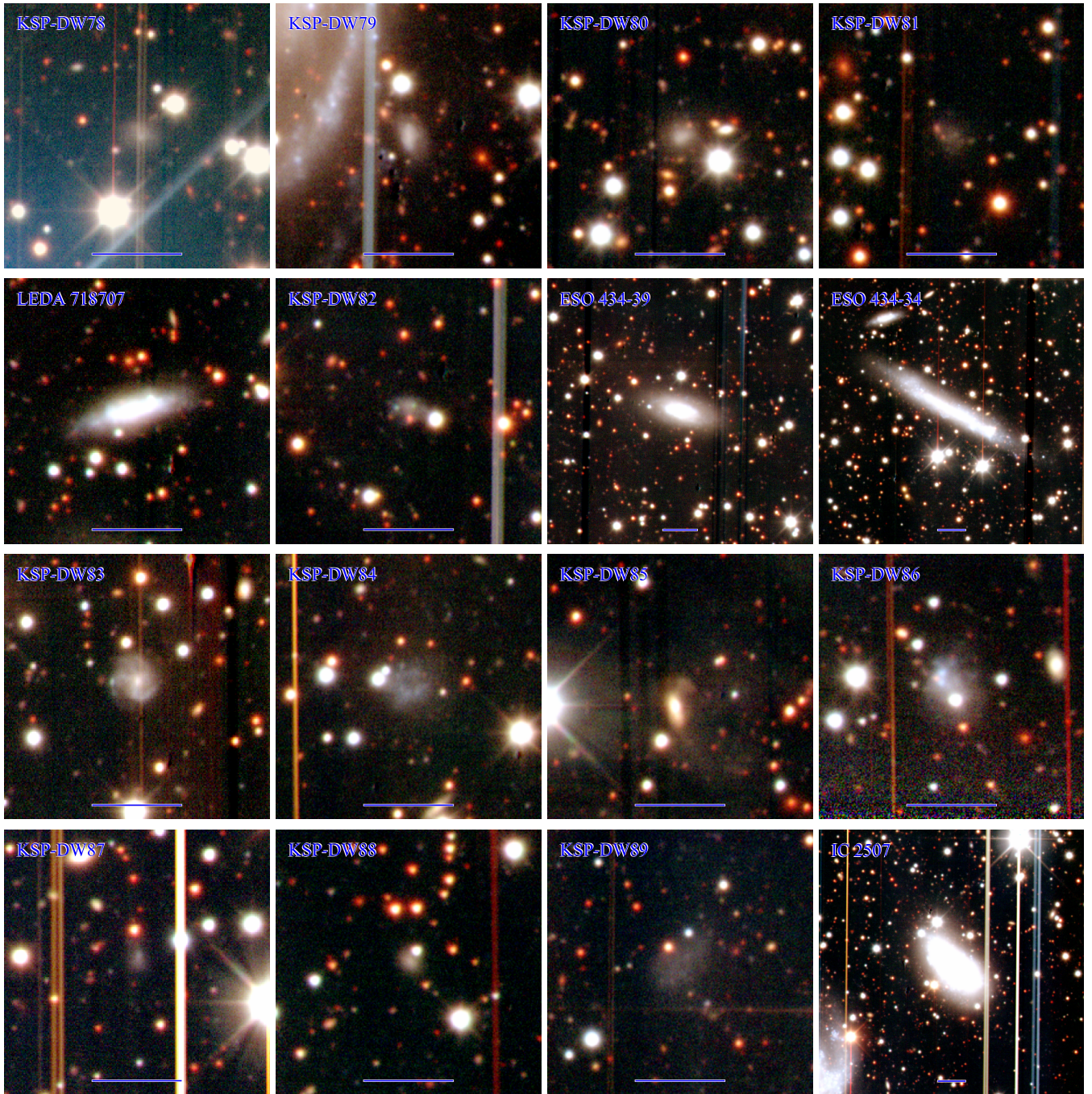
## REFERENCES

- Afsariardchi N., et al., 2019, *ApJ*, **881**, 22  
 Barsanti S., et al., 2018, *ApJ*, **857**, 71  
 Bennet P., Sand D. J., Crnojević D., Spekkens K., Karunakaran A., Zaritsky D., Mutlu-Pakdil B., 2019, *ApJ*, **885**, 153  
 Bennet P., Sand D. J., Crnojević D., Spekkens K., Karunakaran A., Zaritsky D., Mutlu-Pakdil B., 2020, *ApJ*, **893**, L9  
 Bertin E., Mellier Y., Radovich M., Missonnier G., Didelon P., Morin B., 2002, in Bohlender D. A., Durand D., Handley T. H., eds, *Astronomical Society of the Pacific Conference Series Vol. 281, Astronomical Data Analysis Software and Systems XI*. p. 228  
 Bray A. D., et al., 2016, *MNRAS*, **455**, 185  
 Carlsten S. G., Greene J. E., Peter A. H. G., Beaton R. L., Greco J. P., 2021a, *ApJ*, **908**, 109  
 Carlsten S. G., Greene J. E., Greco J. P., Beaton R. L., Kado-Fong E., 2021b, *ApJ*, **922**, 267  
 Carlsten S. G., Greene J. E., Greco J. P., Beaton R. L., Kado-Fong E., 2021c, *ApJ*, **922**, 267  
 Carlsten S. G., Greene J. E., Beaton R. L., Danieli S., Greco J. P., 2022, *ApJ*, **933**, 47  
 Chandrasekhar S., 1943, *ApJ*, **97**, 255  
 Chang R., Gallazzi A., Kauffmann G., Charlot S., Ivezić Ž., Brinchmann J., Heckman T. M., 2006, *MNRAS*, **366**, 717  
 Chattopadhyay T., Debsarma S., Karmakar P., Davoust E., 2015, *New Astron.*, **34**, 151  
 Chiboucas K., Karachentsev I. D., Tully R. B., 2009, *AJ*, **137**, 3009  
 Côté P., et al., 2006, *ApJS*, **165**, 57  
 Crnojević D., et al., 2016, *ApJ*, **823**, 19  
 De Lucia G., Weinmann S., Poggianti B. M., Aragón-Salamanca A., Zaritsky D., 2012, *MNRAS*, **423**, 1277  
 Doyle M. T., et al., 2005, *MNRAS*, **361**, 34  
 Dunn J. M., 2010, *MNRAS*, **408**, 392  
 Fahrion K., et al., 2021, *A&A*, **650**, A137  
 Ferguson H. C., Sandage A., 1988, *AJ*, **96**, 1520  
 Fillingham S. P., Cooper M. C., Boylan-Kolchin M., Bullock J. S., Garrison-Kimmel S., Wheeler C., 2018, *MNRAS*, **477**, 4491  
 Garcia A. M., 1993, *A&AS*, **100**, 47  
 Geha M., Blanton M. R., Yan R., Tinker J. L., 2012, *ApJ*, **757**, 85  
 Geha M., et al., 2017, *ApJ*, **847**, 4  
 Han J., Cole S., Frenk C. S., Jing Y., 2016, *MNRAS*, **457**, 1208  
 Hess K. M., Pisano D. J., Wilcots E. M., Chengalur J. N., 2009, *ApJ*, **699**, 76–88  
 Janz J., Lisker T., 2009, *ApJ*, **696**, L102  
 Jester S., et al., 2005, *AJ*, **130**, 873

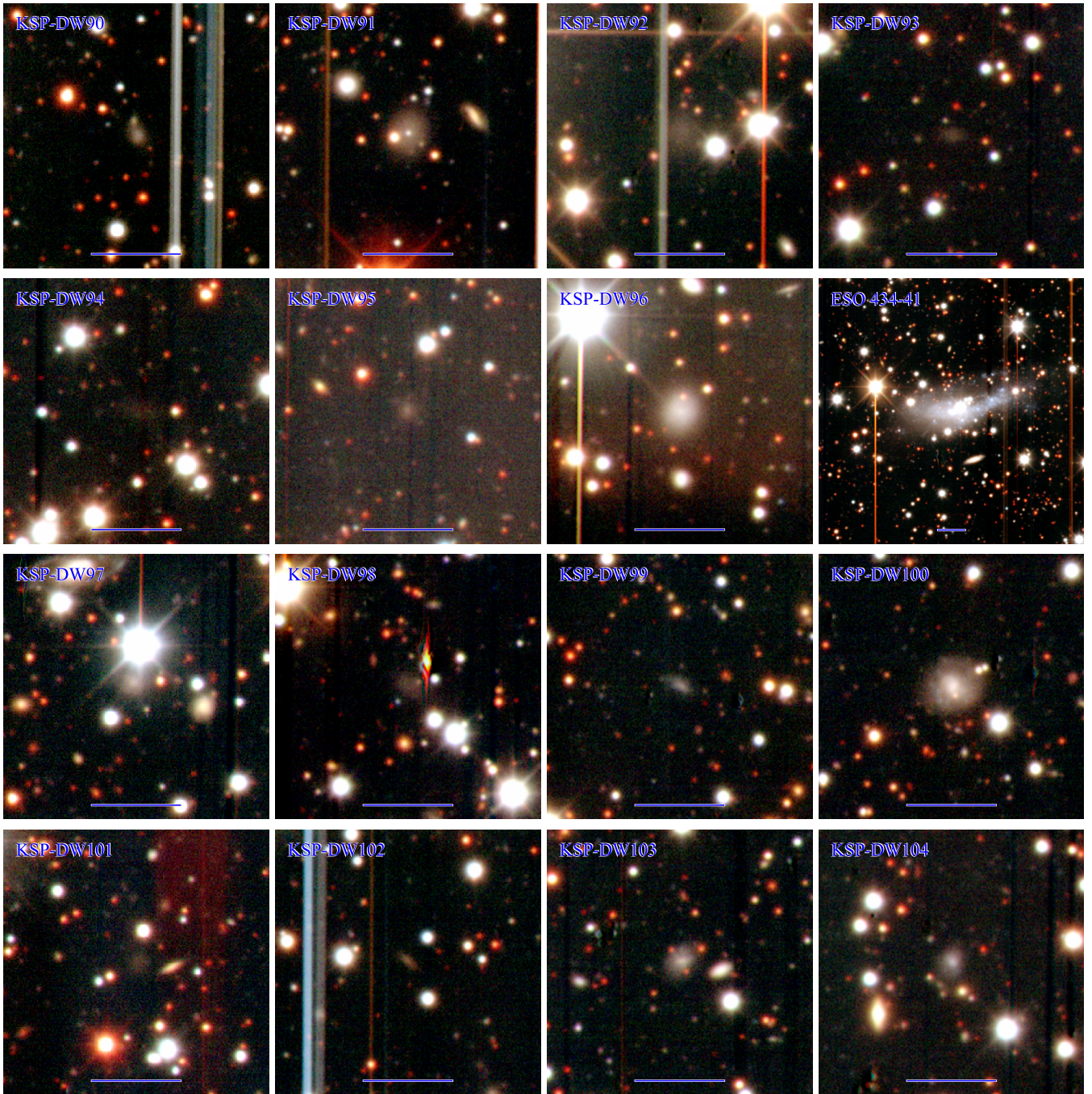
- Jiang C. Y., Jing Y. P., Faltenbacher A., Lin W. P., Li C., 2008, *ApJ*, **675**, 1095
- Jones D. H., et al., 2009, *MNRAS*, **399**, 683
- Jones M. G., Bennet P., Mutlu-Pakdil B., Sand D. J., Spekkens K., Crnojević D., Karunakaran A., Zaritsky D., 2021, *ApJ*, 919, 72
- Joshi G. D., Parker L. C., Wadsley J., 2016, *MNRAS*, **462**, 761
- Kafle P. R., et al., 2016, *MNRAS*, **463**, 4194
- Khalifeh A. R., Jimenez R., 2021, *MNRAS*, **501**, 254
- Kim S.-L., et al., 2016, *Journal of Korean Astronomical Society*, **49**, 37
- Kim S., Contini E., Choi H., Han S., Lee J., Oh S., Kang X., Yi S. K., 2020, *ApJ*, **905**, 12
- Kirby E. N., Cohen J. G., Guhathakurta P., Cheng L., Bullock J. S., Gallazzi A., 2013, *ApJ*, **779**, 102
- Klypin A., Kravtsov A. V., Valenzuela O., Prada F., 1999, *ApJ*, **522**, 82
- Kormendy J., Bender R., 2012, *ApJS*, **198**, 2
- Larsen S. S., Richtler T., 1999, *A&A*, **345**, 59
- Lassen A. E., Riffel R., Chies-Santos A. L., Johnston E., Häußler B., Azevedo G. M., Ruschel-Dutra D., Riffel R. A., 2021, *MNRAS*, **506**, 3527
- Lauberts A., Valentijn E. A., 1989, The surface photometry catalogue of the ESO-Uppsala galaxies
- Lee Y., Rey S.-C., Hilker M., Sheen Y.-K., Yi S. K., 2016, *ApJ*, 822, 92
- Lee Y., Kim S. C., Moon D.-S., Park H. S., Drout M. R., Ni Y. Q., Im H., 2022, *ApJ*, **925**, L22
- Li P., Lelli F., McGaugh S., Pawlowski M. S., Zwaan M. A., Schombert J., 2019, *ApJ*, **886**, L11
- Lisker T., Grebel E. K., Binggeli B., 2007, *AJ*, **135**, 380–399
- Lisker T., Weinmann S. M., Janz J., Meyer H. T., 2013, *Monthly Notices of the Royal Astronomical Society*, **432**, 1162–1177
- Mao Y.-Y., Geha M., Wechsler R. H., Weiner B., Tollerud E. J., Nadler E. O., Kallivayalil N., 2021, *ApJ*, **907**, 85
- Masters K. L., 2005, in 22nd Texas Symposium on Relativistic Astrophysics. pp 374–379 ([arXiv:astro-ph/0503271](https://arxiv.org/abs/astro-ph/0503271))
- Matthews L. D., Gallagher John S. I., Littleton J. E., 1995, *AJ*, **110**, 581
- Meyer M. J., et al., 2004, *MNRAS*, **350**, 1195
- Milliard B., Marcelin M., 1981, *A&A*, **95**, 59
- Moon D.-S., et al., 2016, in Hall H. J., Gilmozzi R., Marshall H. K., eds, Society of Photo-Optical Instrumentation Engineers (SPIE) Conference Series Vol. 9906, Ground-based and Airborne Telescopes VI. p. 99064I, [doi:10.1117/12.2233921](https://doi.org/10.1117/12.2233921)
- Moon D.-S., et al., 2021, *ApJ*, **910**, 151
- Müller O., Jerjen H., Binggeli B., 2015, *A&A*, **583**, A79
- Müller O., Jerjen H., Binggeli B., 2018, *A&A*, **615**, A105
- Ni Y. Q., et al., 2022, *Nature Astronomy*, **6**, 568
- Ni Y. Q., Moon D.-S., Drout M. R., Matzner C. D., Leong K. C. C., Kim S. C., Park H. S., Lee Y., 2023a, *arXiv e-prints*, p. [arXiv:2304.00625](https://arxiv.org/abs/2304.00625)
- Ni Y. Q., et al., 2023b, *ApJ*, **946**, 7
- Oh K. S., Lin D. N. C., 2000, *ApJ*, **543**, 620
- Otter J. A., Masters K. L., Simmons B., Lintott C. J., 2020, *MNRAS*, **492**, 2722
- Park H. S., Moon D.-S., Zaritsky D., Pak M., Lee J.-J., Kim S. C., Kim D.-J., Cha S.-M., 2017, *ApJ*, 848
- Park H. S., Moon D.-S., Zaritsky D., Kim S. C., Lee Y., Cha S.-M., Lee Y., 2019, *ApJ*, **885**, 88
- Pasetto S., Chiosi C., Carraro G., 2003, *A&A*, **405**, 931–949
- Paturel G., Petit C., Prugniel P., Theureau G., Rousseau J., Brouty M., Dubois P., Cambrésy L., 2003, *A&A*, **412**, 45
- Pisano D. J., 2014, *AJ*, **147**, 48
- Pisano D. J., Barnes D. G., Staveley-Smith L., Gibson B. K., Kilborn V. A., Freeman K. C., 2011, *ApJS*, **197**, 28
- Pisano D. J., Barnes D. G., Staveley-Smith L., Gibson B. K., Kilborn V. A., Freeman K. C., 2012, *ApJS*, **201**, 39
- Poulain M., et al., 2021, *MNRAS*, **506**, 5494
- Presotto V., et al., 2012, *A&A*, **539**, A55
- Redd N. T., 2018, *Proceedings of the National Academy of Sciences*, **115**, 12836
- Roberts I. D., Parker L. C., Joshi G. D., Evans F. A., 2015, *MNRAS*, **448**, L1
- Román J., Trujillo I., Montes M., 2020, *A&A*, **644**, A42
- Samuel J., Wetzel A., Santistevan I., Tollerud E., Moreno J., Boylan-Kolchin M., Bailin J., Pardasani B., 2022, *MNRAS*, **514**, 5276
- Schlafly E. F., Finkbeiner D. P., 2011, *ApJ*, **737**, 103
- Sengupta C., Balasubramanyam R., 2006, *MNRAS*, **369**, 360
- Skrutskie M. F., et al., 2006, *AJ*, **131**, 1163
- Springel V., et al., 2008, *MNRAS*, **391**, 1685
- Theureau G., Bottinelli L., Coudreau-Durand N., Gouguenheim L., Hallet N., Loulergue M., Paturel G., Teerikorpi P., 1998, *A&AS*, **130**, 333
- Tremmel M., Wright A. C., Brooks A. M., Munshi F., Nagai D., Quinn T. R., 2020, *MNRAS*, **497**, 2786
- Trentham N., Tully R. B., 2002, *MNRAS*, **335**, 712–732
- Trentham N., Tully R. B., 2009, *MNRAS*, **398**, 722
- Treyer M., et al., 2018, *MNRAS*, **477**, 2684
- Vulcani B., et al., 2013, *A&A*, **550**, A58
- Weinberg D. H., Bullock J. S., Governato F., Kuzio de Naray R., Peter A. H. G., 2015, *Proceedings of the National Academy of Science*, **112**, 12249
- Weinmann S. M., van den Bosch F. C., Yang X., Mo H. J., 2006, *MNRAS*, **366**, 2
- Weisz D. R., et al., 2011, *ApJ*, **739**, 5
- Wetzel A. R., Tinker J. L., Conroy C., van den Bosch F. C., 2013, *MNRAS*, **432**, 336–358
- Zaritsky D., Donnerstein R., Karunakaran A., Barbosa C. E., Dey A., Kadowaki J., Spekkens K., Zhang H., 2021, *ApJS*, **257**, 60
- de Vaucouleurs G., 1979, *ApJ*, **227**, 729
- de Vaucouleurs A., Longo G., 1988, Catalogue of visual and infrared photometry of galaxies from 0.5 micrometer to 10 micrometer (1961-1985)
- van Dokkum P. G., Abraham R., Merritt A., Zhang J., Geha M., Conroy C., 2015, *ApJ*, **798**, L45
- van Dokkum P., et al., 2016, *ApJ*, **828**, L6
- von der Linden A., Wild V., Kauffmann G., White S. D. M., Weinmann S., 2010, *MNRAS*, **404**, 1231

## APPENDIX A: LARGE FIGURES AND TABLES

This paper has been typeset from a  $\text{\TeX}/\text{\LaTeX}$  file prepared by the author.



**Figure A1.** RGB cutout images of the 55 DGCs in Table 4. North is up and east is to the left. The blue horizontal bar at the bottom of each image corresponds to an angular size of  $0.5''$  ( $= 1.77$  kpc at the distance of 12.2 Mpc).

Fig. A1. — *Continued***Table A1.** KMTNet Dwarf Galaxy Discoveries Summary Table

Host Name	Host Type	Distance (Mpc)	$M_B$ (mag)	# of DGCs <sup>a</sup>	$\langle (B - V)_0 \rangle$ (mag)	$C^b$	LF Slope
NGC 2784	SA(s)	9.8	-19.0	38	0.66	-0.12	-1.22
NGC 3585	E7/S0	20.4	-21.0	50	0.69	-0.06	-1.33
NGC 2997	SAB(rs)c	12.2	-20.5	55	0.56	0.40	-1.43

<sup>a</sup>The # of DGCs includes previously discovered dwarf galaxies.<sup>b</sup> $C$  is the linear correlation coefficient, see §4.2.Host type and  $M_B$  information are obtained from Simbad, while the rest are from [Park et al. 2017](#) or [Park et al. 2019](#).

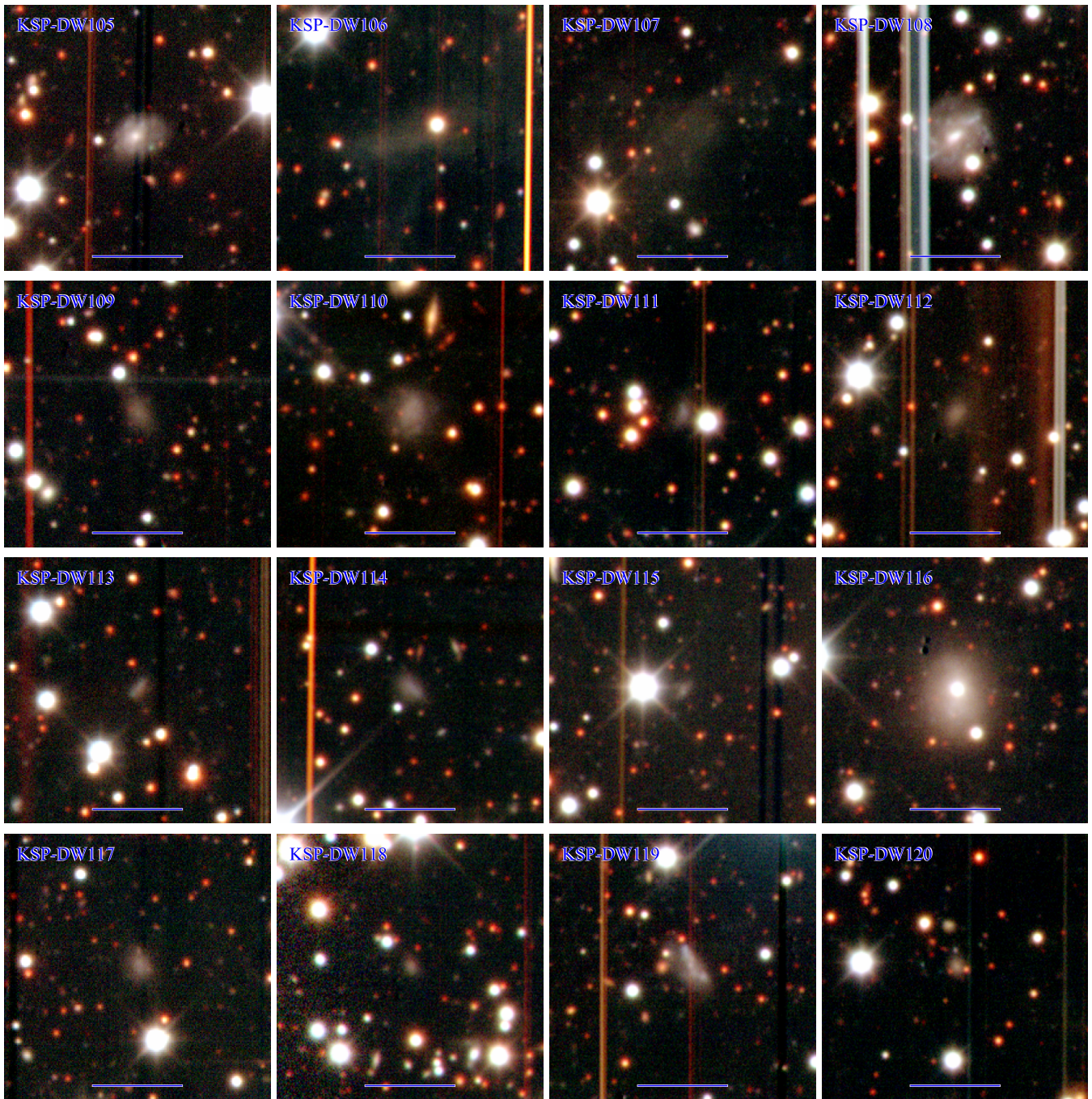


Fig. A1. — *Continued*

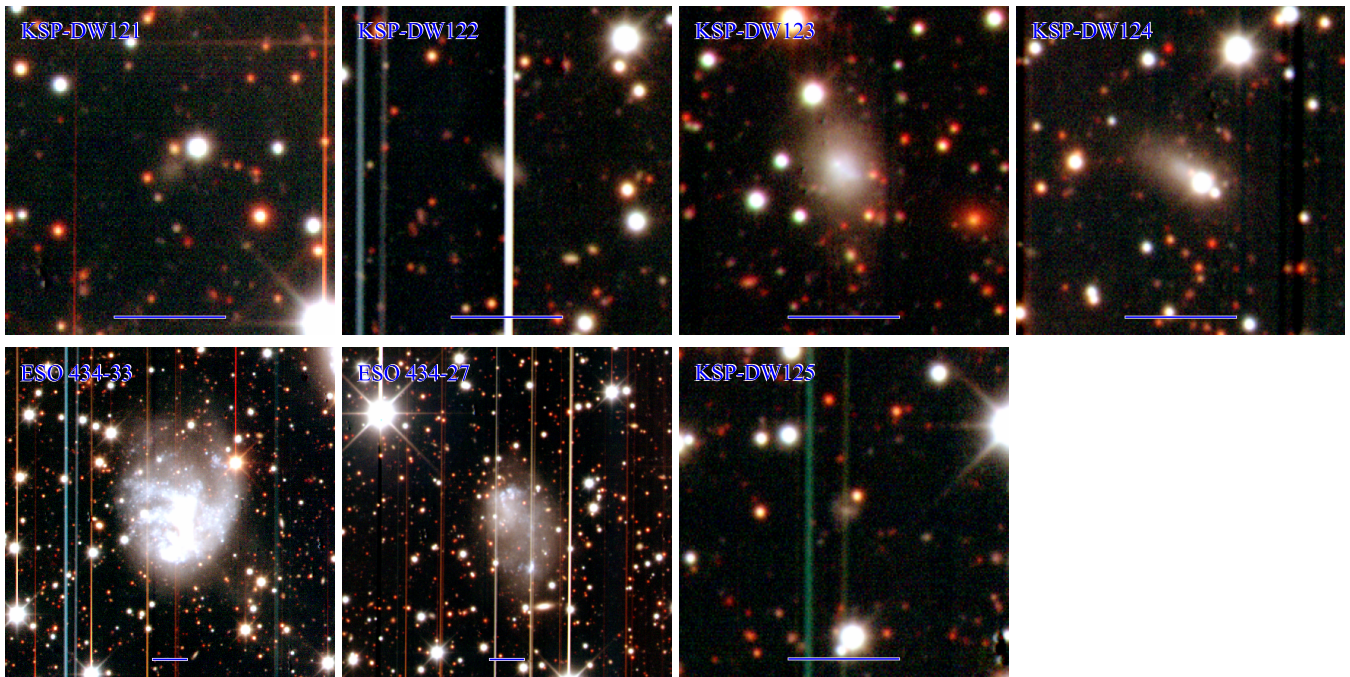
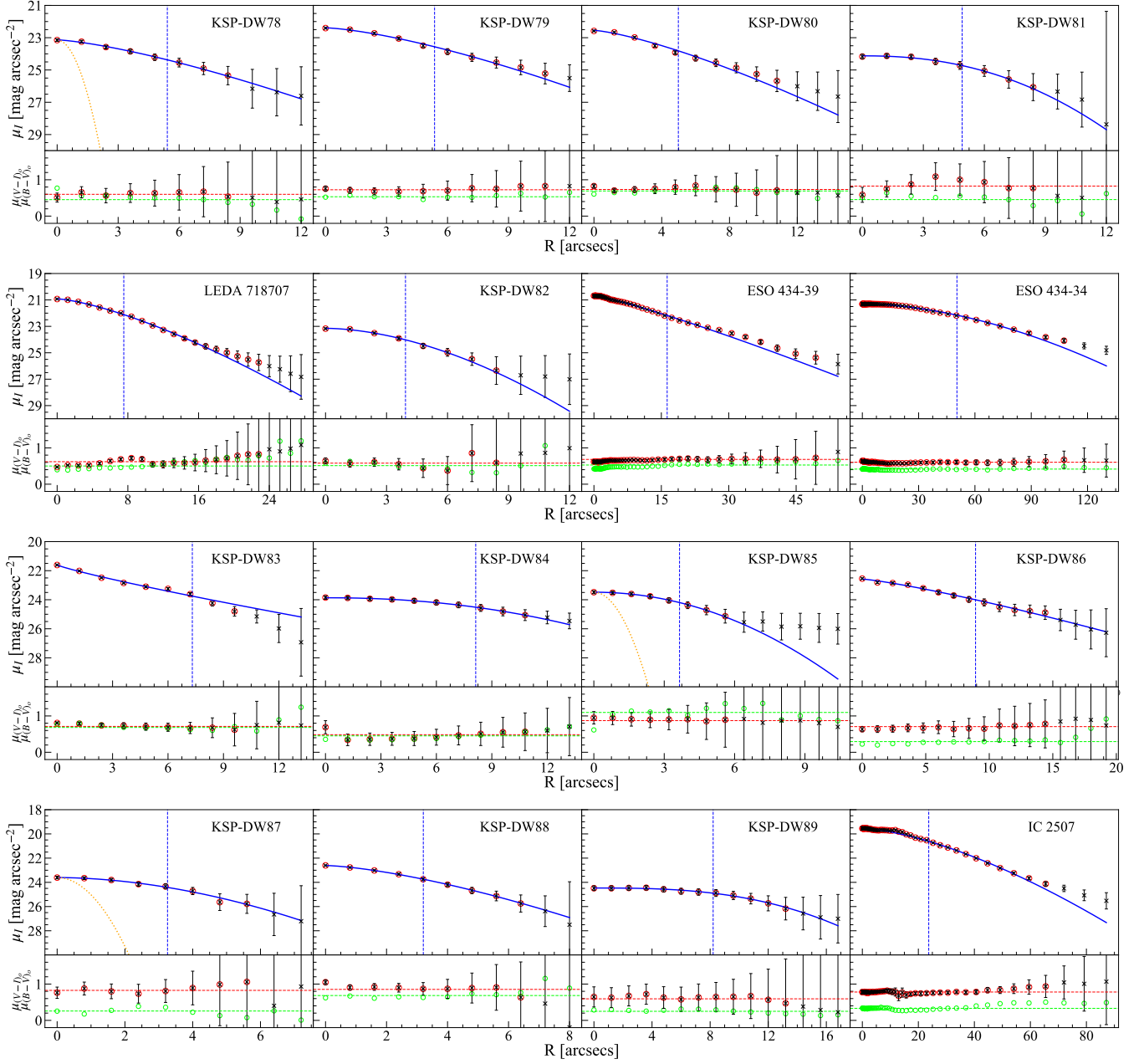
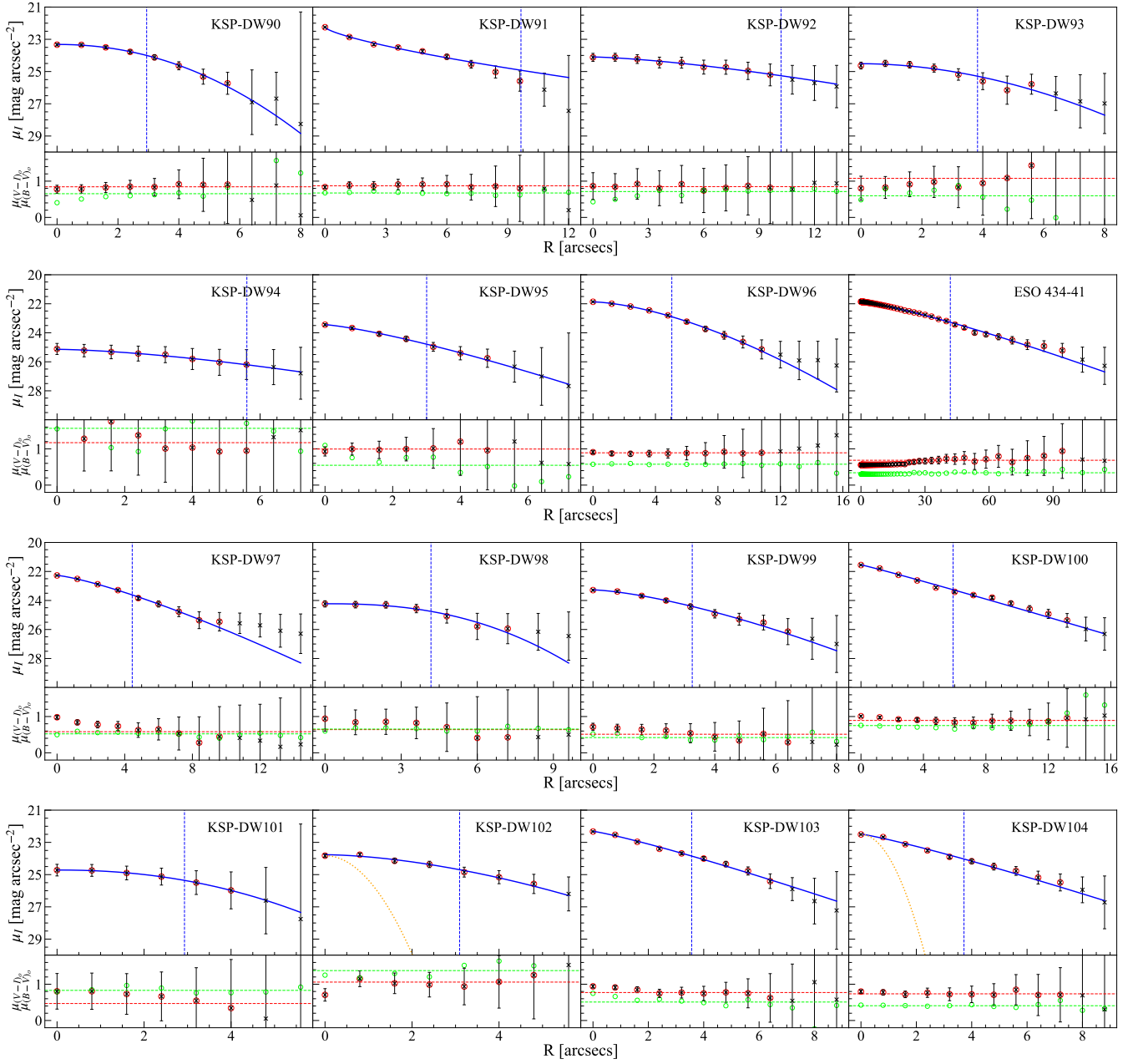


Fig. A1. — *Continued*



**Figure A2.** *Upper Panels:*  $I$ -band surface brightness profiles of the DGCs. The black crosses with error bars, often encircled by a red circle, represent  $\mu_I$  and its uncertainty. Only those data points with a red circle are used in Sérsic fitting. The blue solid curves show the resulting best-fit Sérsic profiles. The vertical blue dashed lines mark the estimated effective radii. *Lower Panels:*  $(B - V)_0$  and  $(V - I)_0$  color profiles are shown in green circles and black crosses, respectively. The green and red horizontal dashed lines represent the mean  $(B - V)_0$  and  $(V - I)_0$  colors obtained from difference in total apparent magnitudes (See § 3.2), respectively. The dotted orange curves in the surface brightness profiles of KSP-DW78, DW85, DW87, DW102, DW104, DW108, DW115, and DW118 are the PSF profiles of the images to which the corresponding DGCs belong, each representing one image (from F1-Q0 to F2-Q3, see Table 2).

Fig. A2. — *Continued*

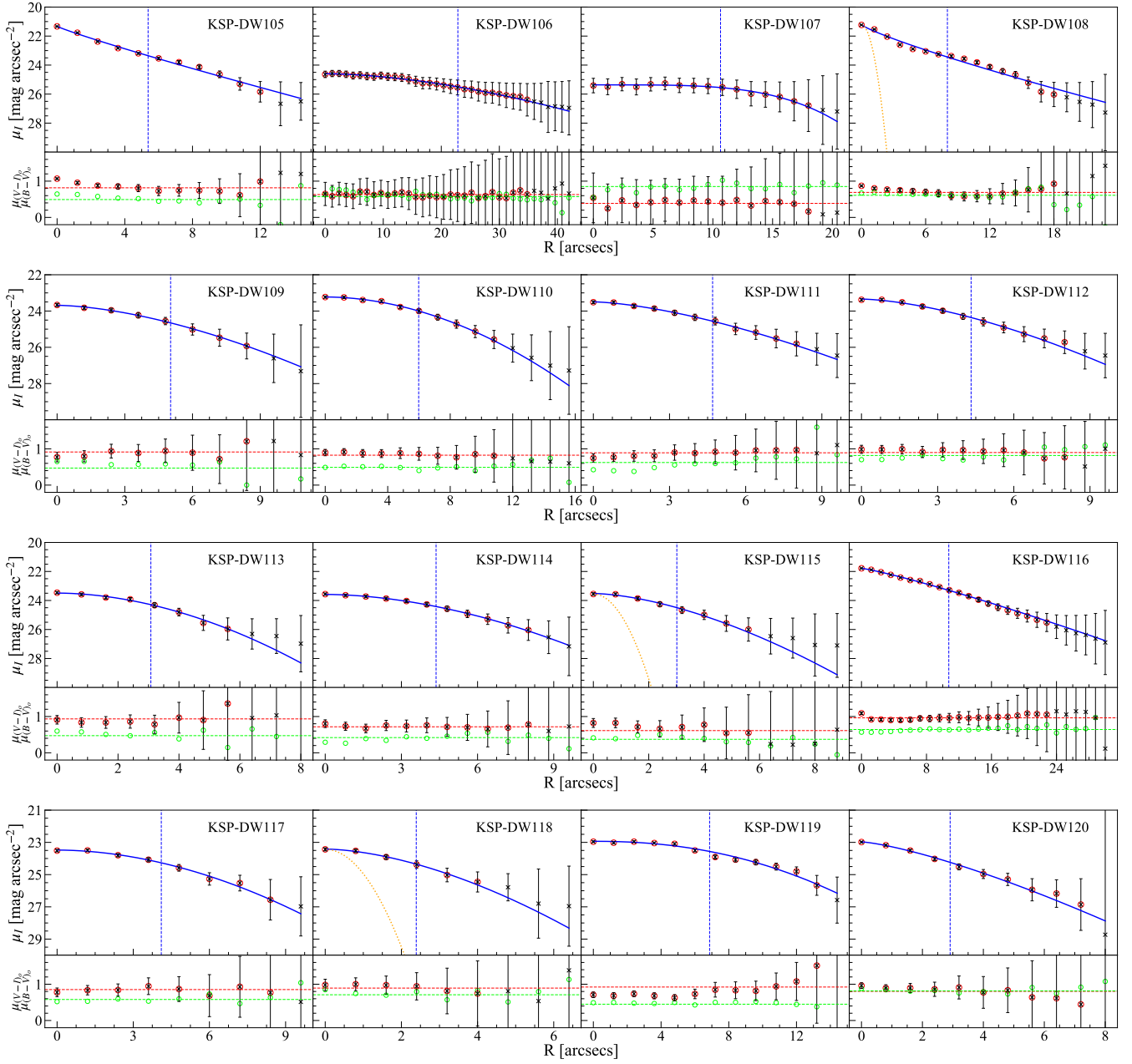


Fig. A2. — Continued

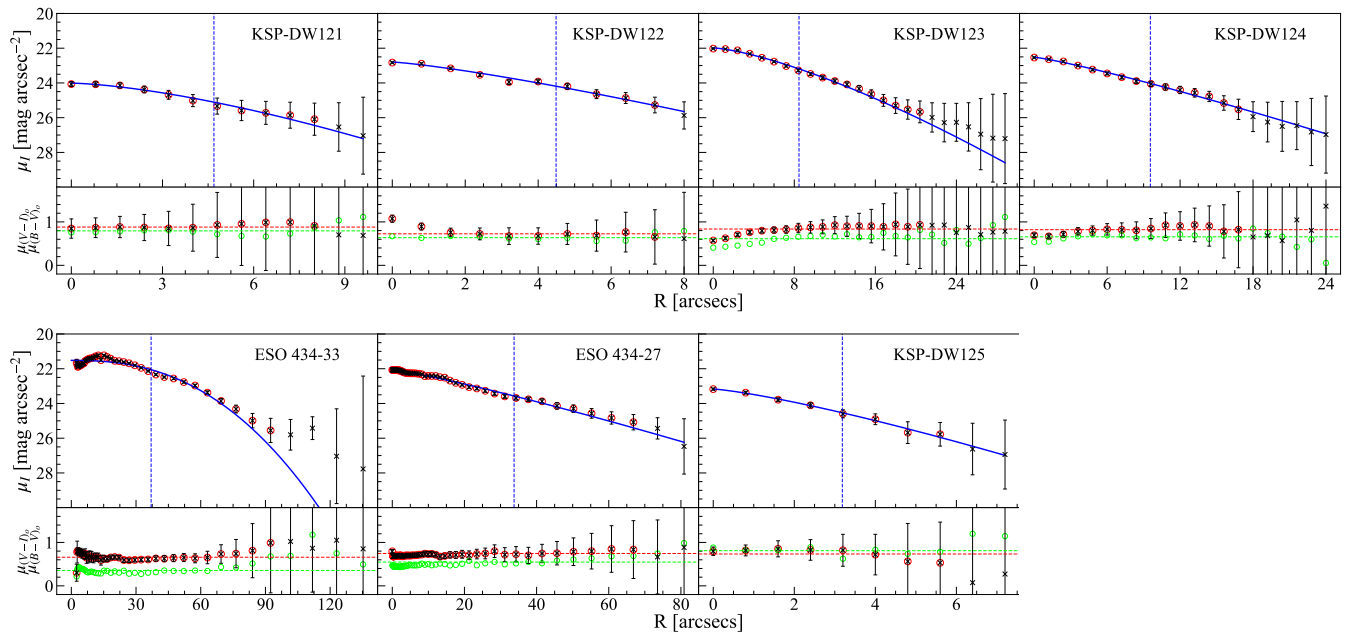


Fig. A2. — *Continued*